Acta Pharmaceutica Sinica B 2026;16(5):3001−3025

Chinese Pharmaceutical Association
Institute of Materia Medica, Chinese Academy of Medical Sciences

Acta Pharmaceutica Sinica B

www.elsevier.com/locate/apsb
www.sciencedirect.com

ORIGINAL ARTICLE

Oridonin as a novel KDM5C inhibitor alleviates clonal hematopoiesis-induced cardiac aging *via* H3K4me3-dependent SASP suppression

Xingling Chen[a,b,c,d,e,†], Qiangqiang Zhao[a,b,c,†], Linhuang Chen[f], Shengrong Lin[a,b,c,d,e], Bin Mai[a,b,c], Xingling He[a,b,c,d,e], Xiaojiao Zhang[a,b,c,d,e], Jiahui Chen[a,b,c,d,e], Sijing Li[a,b,c,d,e], Ziru Li[a,b,c,d,e], Hua Zhang[a,b,c], Yuehui Zhou[a,b,c], Xiaofang Li[a,b,c], Huili Liao[a,c,d,e], Taochun Ye[a,c,d,e,*], Shuning Sun[a,b,c,d,e,*], Zhongqi Yang[a,c,d,e,*], Shihao Ni[a,b,c,d,e,*], Lu Lu[a,b,c,d,e,*]

[a]*The First Affiliated Hospital, Guangzhou University of Chinese Medicine, Guangzhou 510407, China*
[b]*Lingnan Medical Research Center, Guangzhou University of Chinese Medicine, Guangzhou 510407, China*
[c]*Guangdong Clinical Research Institute of Chinese Medicine, Guangzhou 510407, China*
[d]*University Key Laboratory of Traditional Chinese Medicine Prevention and Treatment of Chronic Heart Failure, Guangzhou 510405, China*
[e]*Guangzhou Key Laboratory for Chinese Medicine Prevention and Treatment of Chronic Heart Failure, Guangzhou University of Chinese Medicine, Guangzhou 510405, China*
[f]*Science and Technology Innovation Center, Guangzhou University of Chinese Medicine, Guangzhou 510407, China*

Received 11 June 2025; received in revised form 6 November 2025; accepted 14 January 2026

KEY WORDS

Clonal hematopoiesis;
TET2;
Cardiac aging;
Oridonin;

Abstract *TET2*-mediated clonal hematopoiesis of indeterminate potential (CHIP) is a known cardiovascular risk factor, but its role in cardiac aging and potential for pharmacological intervention remain unclear. Herein, Mendelian randomization using large-scale genome-wide association studies (GWAS) data assessed CHIP's causal impact on aging and cardiovascular disease that revealed significant causal associations between *TET2*-CHIP, CVD, and aging biomarkers. Transcriptome-guided screening identified oridonin as a candidate compound reversing CHIP- and aging-associated gene signatures. Multi-

*Corresponding authors.
E-mail addresses: coinland@gzucm.edu.cn (Lu Lu), Shihao_Ni@163.com (Shihao Ni), yang_zhongqi@163.com (Zhongqi Yang), 15626106630@163.com (Shuning Sun), yetaochun@163.com (Taochun Ye).
[†]These authors made equal contributions to this work.
Peer review under the responsibility of Chinese Pharmaceutical Association and Institute of Materia Medica, Chinese Academy of Medical Sciences.

https://doi.org/10.1016/j.apsb.2026.02.006
2211-3835 © 2026 The Authors. Published by Elsevier B.V. on behalf of Chinese Pharmaceutical Association and Institute of Materia Medica, Chinese Academy of Medical Sciences. This is an open access article under the CC BY-NC-ND license (http://creativecommons.org/licenses/by-nc-nd/4.0/).

KDM5C;
SASP;
Mendelian randomization;
H3K4me3

tiered target prediction combining chemical structure-based algorithms and transcriptomic correlation identified KDM5C as a key target, validated by enzymatic inhibition and surface plasmon resonance assays. *In vivo* and *in vitro* administration of oridonin significantly ameliorated cardiac dysfunction and pathological remodeling in the CHIP model. Epigenetic regulation was profiled *via* ChIP-seq and RNA-seq, focusing on H3K4me3-mediated transcription. *Tet2*$^{+/-}$BMT mice exhibited age-progressive myocardial fibrosis, inflammation, senescence, and functional decline. Mechanistically, oridonin inhibited KDM5C histone demethylase, restored H3K4me3 levels, and activated the SIRT2 anti-aging pathway. Rescue experiments using gene overexpression and recombinant protein supplementation confirmed the functional role of the KDM5C−H3K4me3−SIRT2−S100A8 axis in mediating oridonin's effects. Overall, *TET2*-driven CHIP promotes cardiac aging, as evidenced by human genetic analyses and long-term BMT models. Oridonin, by inhibiting KDM5C and restoring H3K4me3-dependent SIRT2 signaling, mitigates CHIP−induced myocardial aging.

© 2026 The Authors. Published by Elsevier B.V. on behalf of Chinese Pharmaceutical Association and Institute of Materia Medica, Chinese Academy of Medical Sciences. This is an open access article under the CC BY-NC-ND license (http://creativecommons.org/licenses/by-nc-nd/4.0/).

1. Introduction

Aging is a predominant risk factor for cardiovascular diseases, accelerating the progressive deterioration of cardiac structure and function, including hypertrophy, arrhythmogenesis, and diastolic dysfunction[1,2]. These maladaptive changes are frequently accompanied by an increased incidence of angina pectoris, acute coronary syndromes, and heart failure, which shorten healthspan[3]. With the rapid expansion of the global aging population, elucidating the molecular mechanisms underlying cardiac aging is critical for developing innovative preventive and therapeutic strategies targeting age-related cardiovascular conditions[4]. Cardiac aging results from the complex interplay of intrinsic and extrinsic stressors, including chronic inflammation, mitochondrial dysfunction, oxidative damage, telomere attrition, epigenetic dysregulation, and impaired proteostasis[5,6].

As a key link between aging and cardiovascular risk, clonal hematopoiesis of indeterminate potential (CHIP), marked by age-related somatic mutations in hematopoietic stem cells, has garnered increasing attention[7-9]. Mutations in canonical driver genes such as *TET2*, *DNMT3A*, *ASXL1*, *TP53*, and *JAK2* confer selective proliferative advantages, promoting the expansion of mutant clones within the aging bone marrow microenvironment[10-14]. The prevalence of CHIP rises with age and is strongly associated with increased all-cause mortality, largely attributable to its link with cardiovascular disease risk[15,16]. While CHIP has been linked to inflammation-related atherosclerotic cardiovascular diseases such as coronary artery disease and myocardial infarction, its role in cardiac aging remains largely unexplored.

Recent clinical observations suggest that loss-of-function mutations in *TET2* or *DNMT3A* are associated with worse cardiovascular outcomes in patients with atherosclerosis, and those with heart failure (or) with preserved ejection fraction[17-21]. However, direct causal evidence linking CHIP-associated mutations to cardiac or vascular aging in humans remains lacking. Murine models further indicate that *Tet2* or *Dnmt3a* deficiency exacerbates cardiovascular injury responses in conditions such as hyperlipidemia, permanent ligation of the left anterior descending artery, transverse aortic constriction, and chronic angiotensin II infusion[10,11,22]. To date, no evidence has established the effect of CHIP on cardiac aging under physiological, non-injury conditions. Given CHIP's pathogenic contribution to cardiovascular disease and its age-dependency, pharmacological strategies targeting CHIP-related cardiac aging have garnered growing interest.

Oridonin, a bioactive diterpenoid extracted from *Rabdosia rubescens*, has been widely studied for its anti-tumor activity and multi-target molecular actions[23]. Beyond its antiproliferative properties, oridonin exhibits potent anti-inflammatory and anti-fibrotic effects in mice of atherosclerosis, ischemia−reperfusion injury, and angiotensin II-induced ventricular remodeling and cardiac hypertrophy in the context of cardiovascular diseases[24-27]. Nevertheless, its potential to modulate CHIP-associated cardiac aging has not yet been explored.

To elucidate the interaction between CHIP and cardiac aging, we employed a multi-tiered research strategy encompassing human genetic analysis, physiologically relevant animal models, and transcriptome-guided pharmacological screening. First, we conducted Mendelian randomization (MR) based on large-scale genome-wide association studies (GWAS) to infer causal relationships between *TET2* mutations, cardiovascular disease (CVD), and biological aging. Second, we developed a *Tet2*$^{+/-}$ bone marrow transplantation (BMT) mouse model to simulate clonal expansion and assess its impact on cardiac aging, compared to naturally aged controls. This *in vivo* model enabled us to delineate CHIP-specific pathological features under physiological conditions. Third, transcriptomic profiling enabled phenotype-based screening, identifying oridonin as a compound capable of downregulating *Tet2*- and aging-associated signatures. Mechanistic studies further revealed that oridonin inhibits the epigenetic regulator KDM5C and activates anti-aging gene programs in the context of *Tet2*-CHIP. Together, our findings position oridonin as a mechanistically informed candidate for mitigating CHIP-induced cardiac aging.

2. Methods

2.1. Mendelian randomization

To investigate the potential causal relationship between age, CHIP, and CVD, we conducted two-sample MR analyses using publicly available summary-level GWAS data. Genetic instruments for CHIP were derived from the exome-based GWAS of CHIP subtypes published by Kessler et al.[28], which analyzed exome sequencing data from 454,803 UK Biobank participants and identified 27,331 CHIP carriers. CHIP status was defined by the

presence of recurrent, protein-altering somatic mutations in a curated list of 23 genes associated with clonal hematopoiesis, detected using the Mutect2 variant caller (Broad Institute, Cambridge, USA) with stringent quality control filtering. Among these, *DNMT3A*, *TET2*, *ASXL1*, *PPM1D*, *TP53*, *JAK2*, *SRSF2*, and *SF3B1* were selected for subtype-specific analyses because they represent the most frequently mutated driver genes in CHIP and exhibit distinct patterns of clonal behavior and disease association. For each CHIP subtype, summary statistics of germline variants associated with the presence of gene-specific somatic mutations were extracted from the corresponding GWAS. Variants that reached genome-wide significance ($P < 5 \times 10^{-8}$) and passed linkage disequilibrium pruning ($r^2 < 0.01$ within 10 Mb) were selected as instrumental variables. Summary statistics for age were obtained from a meta-analysis of GWAS of DNA methylation-based biomarkers of aging, including GrimAge and PhenoAge acceleration, as reported by McCartney et al.[29]. Summary statistics for major cardiovascular outcomes, including coronary artery disease, ischemic stroke, and heart failure, were derived from large-scale exome-wide association studies using UK Biobank data, as described by Backman et al.[30]. MR analyses were conducted using the TwoSampleMR package (version 0.5.6; MRC Integrative Epidemiology Unit, Bristol, UK) in R (R Foundation for Statistical Computing, Vienna, Austria). The primary method was inverse-variance weighted estimation, complemented by MR-Egger regression, weighted median estimation, and MR-PRESSO to test for pleiotropy and outliers. SNPs were harmonized across exposure and outcome datasets, and ambiguous palindromic SNPs were excluded. Cochran's *Q* test was used to assess heterogeneity. Causal estimates were reported with 95% confidence intervals and interpreted in the context of specific CHIP subtypes to assess which gene-mediated CHIP mutations are most strongly associated with age and cardiovascular risk.

2.2. Transcriptome-based screening of natural compounds

To identify natural compounds with potential therapeutic effects on aging, we conducted a transcriptome-based screening strategy in accordance with our previous studies[31-35], using four gene sets: genes upregulated or downregulated in *Tet2*-deficient CHIP and genes similarly dysregulated in aging-related signatures. Differential gene expression profiles were derived from both our *Tet2*$^{-/-}$ models and publicly available aging transcriptomes. Using our curated transcriptomic reference library comprising 152 natural small molecules, we calculated enrichment scores for each compound in relation to these four gene sets. Each compound was evaluated for its ability to reverse disease- and aging-associated transcriptional changes. Specifically, compounds with negative enrichment scores for upregulated genes and positive enrichment scores for downregulated genes, across both the *Tet2*-deficient and aging datasets, were considered as potential anti-aging candidates. This reversal-based scoring approach reflects the compound's potential to normalize pathological transcriptomic signatures. Compounds meeting these criteria consistently across all four gene sets were prioritized for further validation.

2.3. Molecular docking and dynamics simulations

Molecular docking between KDM5C and oridonin was conducted in AutoDock Vina v1.2.5 (The Scripps Research Institute, La Jolla, USA), focusing on the JmjC domain as the binding site. Protein and ligand structures were prepared using MGLTools 1.4.2 (The Scripps Research Institute, La Jolla, USA) with Gasteiger charges assigned; oridonin's 3D conformation was built using Open Babel 3.0 (The Open Babel Development Team, Pittsburgh, USA). A 20 Å × 20 Å × 20 Å docking box was defined, producing 20 binding poses ranked by affinity scores, from which the top pose was selected for analysis. Molecular dynamics simulations were performed using GROMACS 2023.2 (The GROMACS Development Team, Uppsala, Sweden). The Amber99SB-ILDN force field was used for KDM5C, and ligand parameters, including AM1-BCC charges, were generated using AmberTools (University of California, San Francisco, USA) and GAFF (University of California, San Francisco, USA). The system was solvated in a TIP3P triclinic water box, with cutoffs of 1.0 nm for electrostatic and van der Waals interactions. PME was used for long-range electrostatics with a 2 fs timestep at 303.15 K and 1 bar. After energy minimization, 200 ps NVT and 100 ps NPT equilibration were followed by a 100 ns production run. Analyses were performed using GROMACS tools, gmx_MMPBSA (The gmx_MMPBSA development team, Seville, Spain), and custom Python (Python Software Foundation, Wilmington, USA).

2.4. Histone demethylase (KDM5A/B/C/D) activity assay

The enzymatic activity of KDM5A/B/C/D (JARID1 family histone H3K4 demethylases) was determined using a JARID Demethylase Activity/Inhibition Assay Kit (Colorimetric) (IVDSHOW, Wuhan, China). Purified recombinant KDM5A, KDM5B, KDM5C, and KDM5D proteins were used as input enzymes. An H3K4-trimethylated peptide substrate pre-coated onto 8-well strip plates was incubated with each purified KDM5 protein in assay buffer containing required cofactors at 37 °C for 90 min (following the manufacturer's protocol). Demethylated products were captured by a specific anti-demethylated H3K4 antibody, detected with a secondary detection antibody, and visualized by color development. Absorbance at 450 nm was measured using a microplate reader, and demethylase activity was quantified based on the standard curve generated from H3K4-demethylation standards supplied with the kit. The kit measures total demethylase activity toward H3K4me3 and is applicable to the JARID1/KDM5 family (KDM5A−D).

2.5. Surface plasmon resonance (SPR)

SPR assays were performed at 25 °C on a Biacore 1K (Cytiva, Uppsala, Sweden) using Series S Sensor Chip CM5 (Cytiva). KDM5C protein was immobilized *via* amine coupling after activation with 1-ethyl-3-(3-dimethylaminopropyl) carbodiimide and *N*-hydroxysuccinimide at 10 μL/min for 420 s. The immobilization buffer was 10 mmol/L sodium acetate (pH 5.0). A reference flow cell was prepared in parallel without protein. Oridonin was diluted in phosphate-buffered saline containing 5% dimethyl sulfoxide to a series of concentrations and injected at 30 μL/min for 150 s. After each cycle, chip regeneration was performed with 10 mmol/L glycine-HCl (pH 2.0) for 5 min. Binding kinetics were analyzed using Biacore Insight Evaluation Software (version 2.0, Cytiva), fitting data to a 1:1 Langmuir binding model. Sensorgrams were double-referenced by subtracting the signals from the reference cell and blank buffer injections.

2.6. Experimental animals and drug administration

SPF-grade C57BL/6J mice were obtained from the Guangdong Medical Laboratory Animal Center (Guangzhou, China).

Additionally, SPF-grade *Tet2*$^{+/-}$ and B6.SJL-Ptprca/BoyAiTac (Pep Boy) mice were purchased from Guangdong Yaokang Biotechnology Co., Ltd. (Guangzhou, China). All procedures were conducted in accordance with the NIH Guide for the Care and Use of Laboratory Animals and approved by the Ethics Committee of Guangzhou University of Chinese Medicine (Approval No. 20241202002). Non-myeloablative BMT was performed as previously described[19,36]. Briefly, Pep Boy mice received bone marrow cell suspensions from *Tet2*$^{+/+}$ or *Tet2*$^{+/-}$ donor mice. Unfractionated bone marrow cells (5×10^6 cells/day) were injected *via* the retro-orbital vein into non-irradiated recipient mice for 3 consecutive days (total dose, 1.5×10^7 cells). Eight weeks after BMT, mice were observed and monitored for 12 months. Oridonin (Ori; 98% purity) was purchased from Chengdu Manst Biotechnology Co., Ltd. (Chengdu, China). Mice received oral gavage of oridonin at low (20 mg/kg) or high (40 mg/kg) doses, Dapagliflozin (3 mg/kg/day; AstraZeneca, Cambridge, UK) was used as a positive control. All mice received daily oral gavage of 0.2 mL for 2 months.

2.7. Adeno-associated virus vectors construction and production

The coding sequences of mouse *Kdm5c* and *S100a8* were obtained from the *cDNA* library of Genechem (Shanghai, China).

For KDM5C overexpression, a dual-vector split AAV9 system was constructed to accommodate the full-length gene based on homologous recombination sequences (F1/F2, 500 bp overlap). The 5′ fragment (AAV5′-*KDM5C*) was cloned into the GV388 vector backbone (Genechem, Shanghai, China) (pAAV-CMV-bGlobin-WPRE-hGH polyA) using AgeI and BamHI restriction sites under the control of a CMV promoter. The 3′ fragment (AAV3′-*KDM5C*) was inserted into a CMV-deficient GV388 backbone using BamHI and NheI sites, followed by a synthetic polyA signal.

For S100A8 overexpression, the coding sequence of mouse *S100a8* was cloned into the GV825 vector backbone (Genechem, Shanghai, China) (CMV-MCS-3Flag-FT2A-EGFP-WPRE-BGH polyA; Shanghai Genechem Co., Ltd.) using AgeI and NheI restriction enzymes *via* an In-Fusion recombination method (Takara Bio, Kusatsu, Japan).

All recombinant plasmids were verified by DNA sequencing by the supplier (Genechem, Shanghai, China) prior to AAV packaging. Recombinant AAV9 particles were produced by triple transfection of HEK293T cells with the respective expression plasmid(s) together with pHelper and pRepCap helper plasmids using Lipofectamine 2000 (Invitrogen, Carlsbad, USA). Seventy-two hours post-transfection, viral particles were harvested and purified by iodixanol gradient ultracentrifugation followed by ultrafiltration concentration. Viral titers were quantified using a quantitative PCR (qPCR)-based method, and all preparations were formulated in 0.001% Poloxamer 188 (Pluronic F-68; Caisson Laboratories, Smithfield, USA). All AAV preparations were stored at −80 °C until use.

2.8. Lentiviral vector construction and production

Short hairpin RNA (shRNA) sequences targeting mouse *Kdm5c* (GCCTGATCTCCTTCACCAACT) or *Tet2* (GGATGCAAAC GGGAAACAAAC), as well as a non-targeting negative control (TTCTCCGAACGTGTCACGT), were synthesized and cloned into the GV493 vector (hU6-MCS-CBh-gcGFP-IRES-puromycin; Shanghai Genechem Co., Ltd., Shanghai, China) using AgeI and EcoRI restriction sites. All recombinant plasmids were verified by DNA sequencing by the supplier (Genechem, Shanghai, China). For lentivirus production, 293T cells were co-transfected with the shRNA-expressing vector and the packaging plasmids psPAX2 and pMD2.G using Lipofectamine 2000. After 72 h, the culture supernatant containing infectious lentiviral particles was collected, centrifuged briefly to remove cell debris, and filtered through 0.45 μm cellulose acetate membranes. Viral titers were determined by quantitative PCR and were approximately 1×10^9 transducing units (TU)/mL. All lentiviral preparations were stored at −80 °C until use.

2.9. Echocardiographic assessment of cardiac function

The cardiac function of transthoracic echocardiography was evaluated by the Vevo 2100 Imaging System (VisualSonics Inc, Toronto, Canada). In brief, mice were anesthetized by the inhalation of 2% isoflurane. Chest fur was removed with a chemical hair remover, and ultrasound gel was applied. Heart rate was maintained at approximately 450−550 bpm. Cardiac systolic function index included the LV fractional shortening (LVFS), left ventricular ejection fraction (LVEF), end-diastolic LV internal dimension (LVIDd), and end-systolic LV internal dimension (LVIDs) was measured from M-mode images of the short axis view. Diastolic function was quantified by calculating the early/atrial (E/A) filling ratio. Analysis was performed using Vevo Lab Software (VisualSonics Inc).

2.10. Tissue collection and processing

Heart tissues were harvested from mice individually, and all samples were processed in parallel on separate days. After transcardial perfusion with cold PBS, the hearts were excised and dissected to isolate the left ventricular region based on anatomical landmarks. For histological analysis, left ventricular tissue was fixed in 4% paraformaldehyde (PFA; Sigma−Aldrich, St. Louis, USA) at 4 °C overnight and embedded in Paraplast paraffin (Leica Biosystems, Wetzlar, Germany). The remaining tissue from the same heart was immediately snap-frozen in liquid nitrogen and stored at −80 °C for subsequent RNA, protein, or other molecular analyses. Tissues were allocated into parallel batches for histology, qPCR, and Western blotting to ensure consistency across experiments.

2.11. Antibodies

Anti-CTNT antibody (Abiowell, Changsha, China; AWA10274; 1:500 dilution), anti-GH2AX antibody (Abiowell, AWA01860; 1:200 dilution), anti-P21 antibody (Abiowell, AWA59127; WB 1:1000, IHC 1:200), anti-IL1B antibody (Abiowell, AWA10288; 1:500 dilution), anti-TNFA antibody (Abiowell, AWA10207; 1:500 dilution), anti-S100A8 antibody (Abiowell, AWA59228; 1:100 dilution), anti-S100A9 antibody (Abiowell, AWA61078; 1:200 dilution), anti-P16 antibody (Abiowell, AWA13166; 1:200 dilution), anti-P53 antibody (Abiowell, AWA13761; 1:100 dilution), anti- COL1 antibody (Abiowell, AWA00725; 1:300 dilution), anti-ACTB antibody (Abiowell, AWA80001; 1:10,000 dilution), anti-α-smooth muscle actin (α-SMA) antibody (Abiowell, AWA10574; 1:500 dilution), anti-KDM5C antibody (Abcam, Cambridge, UK; ab72152; 1:3000 dilution), anti-F4/80 antibody (Abcam, ab6640; 1:500 dilution), Phalloidin-iFluor 488 (Abcam,

ab176753), Goat Anti-Rabbit IgG (H + L) (Alexa Fluor 488-conjugated) (Elabscience, Wuhan, China; E-AB-1055; 1:300 dilution), Goat Anti-Mouse IgG (H + L) (Alexa Fluor 488-conjugated) (Elabscience, E-AB-1056; 1:300 dilution), Goat Anti-Rabbit IgG (H + L) (Cyanine3-conjugated) (Elabscience, E-AB-1010; 1:100 dilution), and Goat Anti-Mouse IgG (H + L) (Cyanine3-conjugated) (Elabscience, E-AB-1011; 1:100 dilution).

2.12. Primary cell isolation and co-culture

Primary cardiomyocytes and cardiac fibroblasts were isolated from the hearts of 6 to 8-week-old C57BL/6 mice, as previously described[34,37]. Bone marrow cells were collected from the femurs and tibias of mice that had undergone BMT. To induce macrophage differentiation, bone marrow cells were cultured in Dulbecco's modified Eagle's medium supplemented with 10% fetal bovine serum (ExCell Bio, Taicang, China), 1% penicillin−streptomycin, and macrophage colony-stimulating factor (M-CSF) for 7 days. The resulting primary macrophages were then co-cultured with treatments with cardiomyocytes or fibroblasts in Transwell inserts (Corning, NY, USA) to allow paracrine interaction without direct cell contact. All cultures were maintained at 37 °C in a humidified incubator with 5% CO_2.

2.13. CCK-8 cell viability assay

To assess cell viability, cells were seeded into 96-well plates at a density of 0.5×10^4 cells per well in 200 μL of culture medium. Various concentrations of oridonin were subsequently added. Each treatment group was set up in six replicates. At 24, 48, and 72 h, 10 μL of Cell Counting Kit-8 (Dojindo Molecular Technologies, Kumamoto, Japan) solution was added to each well and incubated in the dark for 2 h. Absorbance was measured at 450 nm using an Infinite F50 microplate reader (Tecan, Männedorf, Switzerland). Cell viability was calculated using Eq. (1):

$$\text{Viability (\%)} = (\text{AEX}-\text{AOE})/(\text{ANC}-\text{AOE}) \times 100 \quad (1)$$

2.14. Proteome profiler mouse cytokine array kit

The relative expression of cytokines in macrophage supernatants was profiled using the Proteome Profiler Mouse Cytokine Array Panel A (R&D Systems, Minneapolis, USA) according to the manufacturer's instructions. Briefly, cell culture supernatants from wild-type (WT)-BMT and *Tet2*$^{+/-}$BMT bone marrow−derived macrophages (BMDMs) were centrifuged to remove debris and incubated with a cocktail of biotinylated detection antibodies. The mixtures were then applied to nitrocellulose membranes pre-spotted with 40 different capture antibodies in duplicate. After overnight incubation at 4 °C, membranes were washed and incubated with streptavidin−horseradish peroxidase (HRP), followed by chemiluminescent detection reagents. The resulting signals were visualized on X-ray film, and pixel intensities were quantified using ImageJ software (National Institutes of Health, Bethesda, USA).

2.15. Collagen gel contraction assay

Cell contraction assays were performed using the CytoSelect 24-Well Cell Contraction Assay Kit (Cell Biolabs, Inc, San Diego, USA) following the manufacturer's instructions. Primary mouse cardiac fibroblasts were resuspended at 2×10^6−5×10^6 cells/mL in culture medium. The cell contraction matrix was prepared by mixing 2 parts of cell suspension with 8 parts of cold collagen gel working solution, avoiding air bubbles. 0.5 mL of the mixture was added to each well and polymerized at 37 °C, 5% CO_2 for 1 h. Subsequently, 1.0 mL of culture medium (with/without drug) was added. Gel contraction was monitored for 2 days and quantified using ImageJ.

2.16. Calcium transient imaging in cardiomyocytes

To measure calcium release, cardiomyocytes were seeded onto coverslips as single cells. Following drug treatment, cells were incubated with 5 μmol/L Fluo-4 AM (Invitrogen, Carlsbad, USA) at 37 °C for 10 min, followed by washing. Calcium release events were recorded using an Olympus FV1200 confocal microscope (Olympus, Tokyo, Japan) in line-scan mode. Calcium imaging data were analyzed using FV10-ASW Viewer software (version 4.1; Olympus).

2.17. Seahorse-based mitochondrial function assay

Mitochondrial respiration was assessed by measuring the oxygen consumption rate (OCR) using the Seahorse XF Cell Mito Stress Test Kit (Agilent Technologies, Santa Clara, USA) and a Seahorse XF96 Extracellular Flux Analyzer (Agilent Technologies). Cells were seeded on Matrigel-coated (Corning, Tewksbury, USA) XF96 Flux Paks (Agilent Technologies) at a density of 2×10^4 cells per well. One hour prior to the assay, the culture medium was replaced with Seahorse XF DMEM Basal Medium (Agilent Technologies) supplemented with 10 mmol/L glucose, 2 mmol/L glutamine, and 1 mmol/L sodium pyruvate. For the Mito Stress Test, mitochondrial modulators were sequentially injected: 1.5 μmol/L oligomycin, 1 μmol/L FCCP, and 0.5 μmol/L rotenone/antimycin A. OCR values were normalized to cell number per well.

2.18. Senescence-associated β-galactosidase staining

Senescence-associated β-galactosidase (SA-β-Gal) staining was performed using the β-Galactosidase Staining Kit (Abbkine, Wuhan, China) according to the manufacturer's protocol. Primary mouse cardiomyocytes were cultured on 6-well plates, fixed with 4% paraformaldehyde for 15 min, and washed with PBS. Cells were incubated with staining working solution (pH 6.0) at 37 °C in a CO_2-free incubator overnight. After incubation, cells were rinsed with PBS and visualized under a light microscope (BX53; Olympus, Tokyo, Japan). Blue-stained cells were counted as senescent cells, and the percentage of SABGAL-positive cells was calculated.

2.19. Lipofuscin staining

Lipofuscin staining was performed using the BBcellProbe Lipofuscin Detection Kit (BestBio, Shanghai, China), according to the manufacturer's protocol. Primary mouse cardiomyocytes were fixed with 4% paraformaldehyde for 15 min at room temperature, rinsed with distilled water. Cells were incubated with Schmorl's working solution, prepared by mixing ferric chloride solution and potassium ferrocyanide solution at a 9:1 ratio, for 5 min. After sequential dehydration in graded ethanol, xylene clearing, and

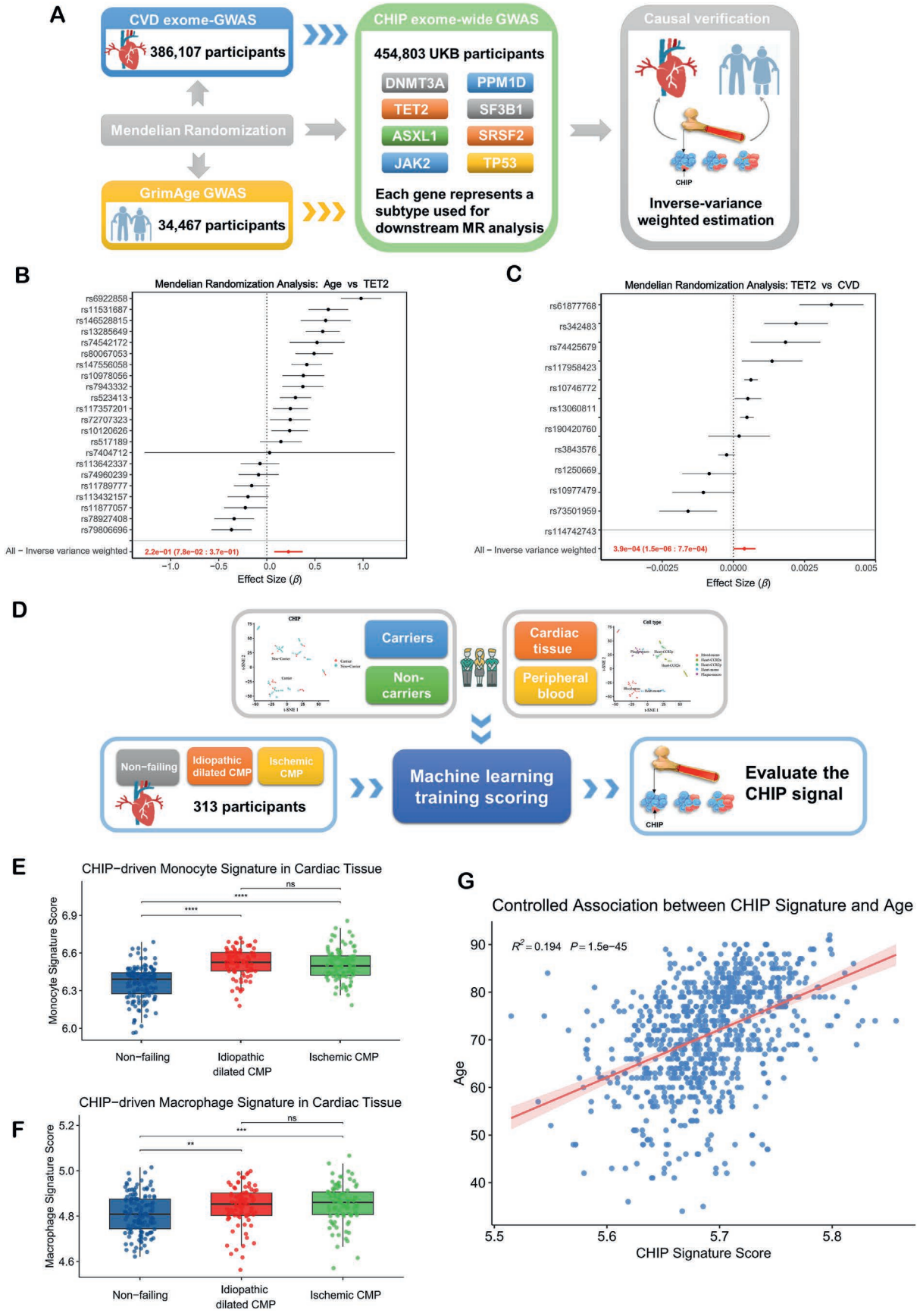
A
CVD exome-GWAS
386,107 participants
Mendelian Randomization
GrimAge GWAS
34,467 participants
CHIP exome-wide GWAS
454,803 UKB participants
DNMT3A
PPM1D
TET2
SF3B1
ASXL1
SRSF2
JAK2
TP53
Each gene represents a subtype used for downstream MR analysis
Causal verification
CHIP
Inverse-variance weighted estimation
B
Mendelian Randomization Analysis: Age vs TET2
rs6922858
rs11531687
rs146528815
rs13285649
rs74542172
rs80067053
rs147556058
rs10978056
rs7943332
rs523413
rs117357201
rs72707323
rs10120626
rs517189
rs7404712
rs113642337
rs74960239
rs11789777
rs113432157
rs11877057
rs78927408
rs79806696
All – Inverse variance weighted
2.2e-01 (7.8e-02 : 3.7e-01)
−1.0
−0.5
0.0
0.5
1.0
Effect Size (β)
C
Mendelian Randomization Analysis: TET2 vs CVD
rs61877768
rs342483
rs74425679
rs117958423
rs10746772
rs13060811
rs190420760
rs3843576
rs1250669
rs10977479
rs73501959
rs114742743
All – Inverse variance weighted
3.9e-04 (1.5e-06 : 7.7e-04)
−0.0025
0.0000
0.0025
0.005
Effect Size (β)
D
CHIP
Carriers
Non-carriers
Cell type
Cardiac tissue
Peripheral blood
Non-failing
Idiopathic dilated CMP
Ischemic CMP
313 participants
Machine learning training scoring
CHIP
Evaluate the CHIP signal
E
CHIP−driven Monocyte Signature in Cardiac Tissue
Monocyte Signature Score
6.0
6.3
6.6
6.9
ns
****
****
Non−failing
Idiopathic dilated CMP
Ischemic CMP
F
CHIP−driven Macrophage Signature in Cardiac Tissue
Macrophage Signature Score
4.6
4.8
5.0
5.2
ns
***
**
Non−failing
Idiopathic dilated CMP
Ischemic CMP
G
Controlled Association between CHIP Signature and Age
R^2 = 0.194 P = 1.5e−45
Age
40
50
60
70
80
90
5.5
5.6
5.7
5.8
CHIP Signature Score

mounting with neutral resin, stained cells were observed and imaged under a light microscope (BX53; Olympus, Tokyo, Japan).

2.20. Flow cytometry for immune and cellular function analysis

Myeloid cells flow cytometry: Myeloid cells were obtained from the spleen by mechanical dissociation through a 70-μm cell strainer, followed by red blood cell lysis and density gradient centrifugation for collection into BD Microtainer tubes containing K2EDTA (BD Biosciences, Franklin Lakes, USA). Red blood cells were lysed using eBioscience 1 × RBC Lysis Buffer (Thermo Fisher Scientific, Waltham, USA) for 5 min on ice. Samples were incubated with fluorochrome-conjugated antibodies for 30 min at room temperature in the dark. Flow cytometry acquisition and gating were performed as previously described[11,19,36]. All antibodies are listed in Supporting Information Table S1.

Measurement of intracellular reactive oxygen species (ROS) in mouse primary cardiomyocytes: to assess ROS, co-cultured and treated cardiomyocytes were incubated with 10 μmol/L DCFH-DA (Beyotime Biotechnology, Shanghai, China) at 37 °C for 30 min, followed by harvesting, washing, and resuspension in PBS. Cells were analyzed by flow cytometry (488 nm excitation, 530/30 nm emission, FITC channel), and fluorescence intensities were normalized to WT controls.

Mitochondrial membrane potential assay in mouse primary cardiomyocytes: primary mouse cardiomyocytes were incubated with 10 μmol/L JC-1 (Beyotime Biotechnology) in JC-1 staining buffer at 37 °C for 20 min. Cells were washed twice with ice-cold staining buffer and resuspended in fresh buffer. Flow cytometry was performed using 488 nm excitation, with emission filters set at 530 ± 15 nm (green, monomeric JC-1) and 585 ± 20 nm (red, J-aggregates). Data were expressed as the ratio of red-to-green fluorescence intensity. Data acquisition was performed using a BD LSRFortessa flow cytometer (BD Biosciences). Flow cytometry data were analyzed using FlowJo software (BD Biosciences).

2.21. Histological and immunofluorescence staining

Paraffin-embedded mouse heart sections (4 μm) were dewaxed in xylene (three changes, 10 min each), rehydrated through graded ethanol (100%−80%), and underwent antigen retrieval in citrate buffer (pH 6.0, 95 °C, 20 min). Endogenous peroxidase was quenched with 3% H_2O_2 (25 min), followed by blocking with 3% BSA in PBS (30 min). Sections were incubated with primary antibodies overnight at 4 °C. For immunofluorescence, after PBS-T washes (3 × 5 min), HRP-conjugated secondaries (1:1000, 50 min) were added, and signal was amplified with the TSA Cyanine 3 System (Akoya Biosciences, Marlborough, USA) (10 min, dark). For dual labeling, additional antigen retrieval (microwave, 8 min on/off/on) was followed by sequential incubation with a second primary antibody and Alexa Fluor 647-conjugated secondary antibody (Thermo Fisher Scientific, Waltham, USA) (1:500, 50 min). Nuclei were counterstained with DAPI (5 μg/mL, 10 min), and autofluorescence was minimized using the TrueVIEW Autofluorescence Quenching Kit (Vector Laboratories, Newark, USA). Slides were mounted with ProLong Diamond Antifade Mountant (Thermo Fisher Scientific). For immunohistochemistry, sections were treated with 3% H_2O_2 (15 min), blocked in 3% goat serum (30 min), and incubated with primary antibodies overnight. HRP-conjugated secondaries were applied (50 min), followed by DAB for color development and hematoxylin for nuclear counterstaining. Sections were dehydrated, cleared, and mounted. Images were acquired using a Nikon A1R confocal microscope (Nikon, Tokyo, Japan).

2.22. Masson's trichrome staining

Mouse heart tissues were fixed in 4% paraformaldehyde, paraffin-embedded, and sectioned (4−5 μm) with a microtome (Leica Microsystems, Wetzlar, Germany). After deparaffinization and graded ethanol rehydration, nuclei were stained with Weigert's hematoxylin (3 min), differentiated in acid alcohol, and blued in tap water. Sections were stained with Biebrich scarlet-acid fuchsin (5−10 min), phosphomolybdic acid (1−3 min), and aniline blue (3−6 min). Following ethanol dehydration, sections were cleared in xylene and mounted. Images were acquired under a BX53 light microscope (Olympus, Tokyo, Japan) and standardized using image software. Collagen-positive fibrotic areas (blue) were quantified by thresholding the aniline blue signal in ImageJ and calculating the collagen-to-myocardium ratio. Staining times were adjusted with 1% acetic acid to ensure optimal contrast.

2.23. Transmission electron microscopy

Heart tissue samples ($\leq$1 mm^3) were fixed in 4 °C electron microscopy fixative (AS1063; Aspen Biological, Wuhan, China) for 2−4 h, washed with PBS (0.1 mol/L, pH 7.4), and post-fixed in 1% OsO_4 for 2 h at room temperature. After PBS washes, samples were dehydrated in graded ethanol, infiltrated with a 1:1 mixture of acetone and epoxy resin, then with pure resin overnight. Polymerization was carried out at 60 °C for 48 h. Ultrathin sections (60−80 nm) were prepared using a diamond knife (Ultra 45°; Diatome, Nidau, Switzerland) on a Leica UC7 ultramicrotome (Leica Microsystems, Wetzlar, Germany). Sections were stained with 2% uranyl acetate and lead citrate (15 min each), air-dried, and imaged with a Tecnai G2 20 TWIN transmission electron microscope (FEI Company, Hillsboro, USA) (80 kV). Sarcomere length was quantified between Z-lines using ImageJ software.

Figure 1 *TET2*-driven clonal haematopoiesis of indeterminate potential (CHIP) is causally associated with aging and cardiovascular disease. (A) Overview of Mendelian randomization (MR) design integrating CHIP-genome-wide association studies (GWAS) (n = 454,803), CVD-GWAS (n = 386,107), and GrimAge-GWAS (n = 34,467). MR analysis demonstrating a significant causal association of *TET2* mutations with aging (B) and cardiovascular disease (C). (D) Workflow for transcriptomic profiling using myocardial RNA-seq (GSE226642) to derive CHIP signatures, followed by projection into two heart failure cohorts (GSE57338 and GSE181114) and immune cell deconvolution *via* MCPcounter. Expression of CHIP-driven monocyte (E) and macrophage (F) signatures across non-failing, idiopathic dilated, and ischemic CMP tissues. (G) Positive correlation between CHIP score and chronological age. P values was calculated by inverse-variance weighted MR and validated using MR-Egger. Error bars indicate 95% confidence intervals. GWAS, genome-wide association study; CMP, cardiomyopathy; ns, not significant.

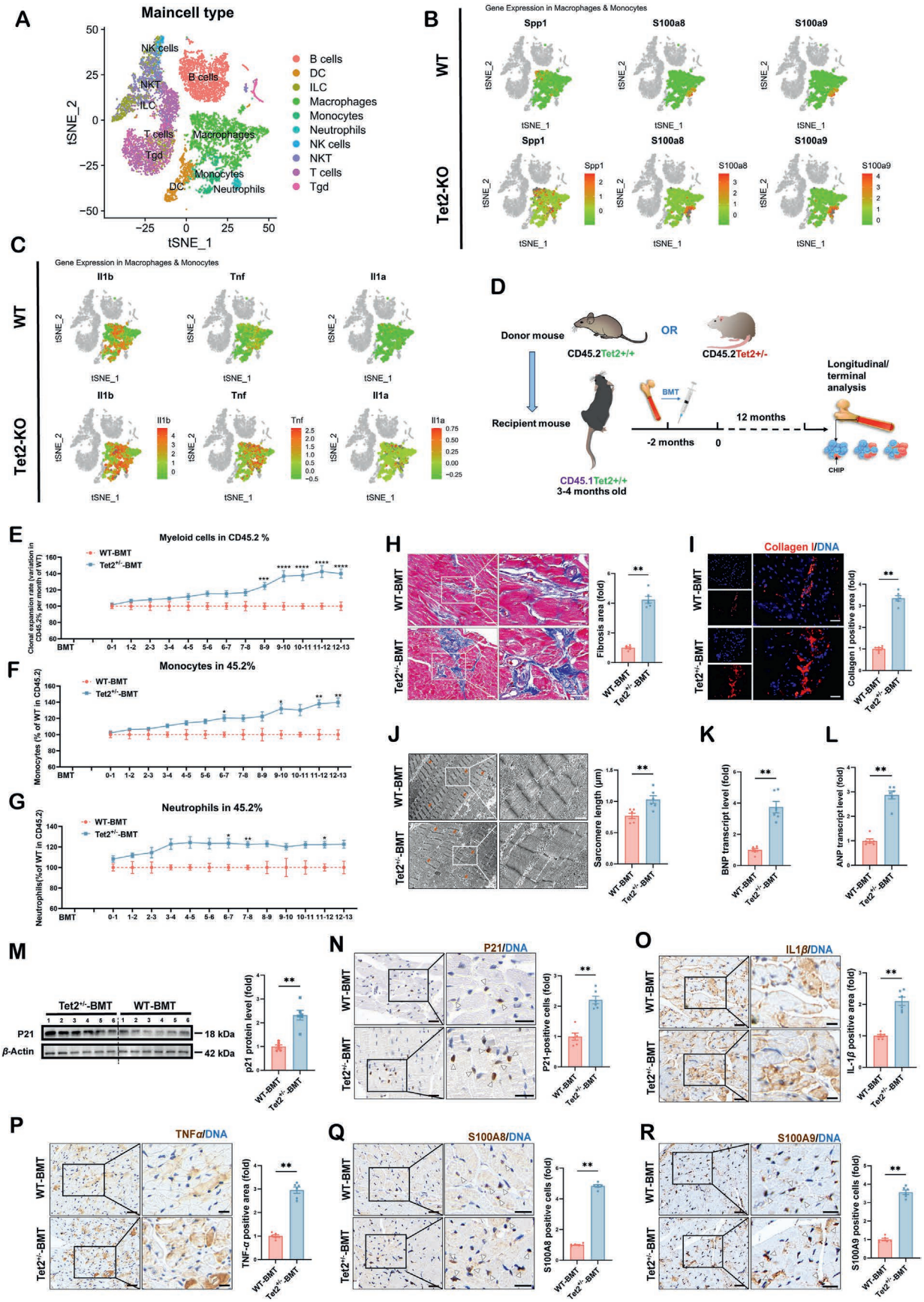
A
Maincell type
B cells
DC
ILC
Macrophages
Monocytes
Neutrophils
NK cells
NKT
T cells
Tgd
tSNE_1
tSNE_2
B
Gene Expression in Macrophages & Monocytes
WT
Tet2-KO
Spp1
S100a8
S100a9
C
Gene Expression in Macrophages & Monocytes
Il1b
Tnf
Il1a
D
Donor mouse
CD45.2Tet2+/+
OR
CD45.2Tet2+/-
Recipient mouse
CD45.1Tet2+/+
3-4 months old
BMT
-2 months
0
12 months
Longitudinal/
terminal
analysis
CHIP
E
Myeloid cells in CD45.2 %
WT-BMT
Tet2+/--BMT
F
Monocytes in 45.2%
G
Neutrophils in 45.2%
H
Fibrosis area (fold)
I
Collagen I/DNA
Collagen I positive area (fold)
J
Sarcomere length (μm)
K
BNP transcript level (fold)
L
ANP transcript level (fold)
M
Tet2+/--BMT
WT-BMT
P21
β-Actin
18 kDa
42 kDa
p21 protein level (fold)
N
P21/DNA
P21-positive cells (fold)
O
IL1β/DNA
IL-1β positive area (fold)
P
TNFα/DNA
TNF-α positive area (fold)
Q
S100A8/DNA
S100A8 positive cells (fold)
R
S100A9/DNA
S100A9 positive cells (fold)

2.24. RNA isolation and RT−qPCR

RNA was extracted after 48 h post-drug treatment. The total RNA of samples was extracted using EZ-press RNA Purification Kit (EZBioscience, Roseville, USA). A 4 × Reverse Transcription Master Mix (EZBioscience) was used for reverse transcription reaction at 42 °C for 15 min, 95 °C for 30 s. The 2 × SYBR Green qPCR Master Mix (EZBioscience) was used to perform qPCR following this protocol: denaturation (5 min, 95 °C), and 40 amplification cycles (10 s at 95 °C, and 30 s at 60 °C) by using the Mx3000P Real-Time PCR System (Agilent Technologies, Santa Clara, USA). Each gene of interest was normalized to *Actb* and the fold change was compared relative to the control sample. The sequences of all primers were listed in Supporting Information Table S2.

2.25. Western blotting

Tissue samples (ground in liquid nitrogen) or cultured cells were lysed in 1 × SDS lysis buffer (62.5 mmol/L Tris-HCl, pH 6.8, 2% SDS) and heated at 105 °C for 10 min. Protein concentrations were measured using Pierce BCA Protein Assay Kit (Thermo Fisher Scientific, Waltham, USA). Equal amounts of protein were separated by SDS-PAGE and transferred onto PVDF membranes. Membranes were blocked with 5% non-fat milk in TBST for 1 h at room temperature, then incubated overnight at 4 °C with primary antibodies. After washing, membranes were incubated with HRP-conjugated secondary antibodies for 1 h at room temperature. Signals were detected using the ChemiDoc XRS Imaging System (Bio-Rad Laboratories, Hercules, USA) with Image Lab Software (Bio-Rad Laboratories).

2.26. Hydroxymethylated DNA immunoprecipitation and sequencing (hMeDIP-seq)

Genomic DNA from mouse cardiac tissues was fragmented to approximately 200−800 bp by sonication. One microgram of fragmented DNA was end-repaired, A-tailed, and ligated to Illumina adapters (Illumina, San Diego, USA). Hydroxymethyl cytosine-containing DNA fragments were immunoprecipitated using an anti-5-hydroxymethylcytosine antibody (Diagenode, Seraing, Belgium), followed by PCR amplification and AMPure XP beads (Beckman Coulter, Brea, USA) purification to obtain ∼300−900 bp libraries. After QC assessment on an Agilent 2100 Bioanalyzer (Agilent Technologies, Santa Clara, USA), libraries were denatured and sequenced on Illumina NovaSeq 6000 (150-bp paired-end mode). Sequencing quality control was performed using FastQC. Reads were adapter-trimmed and mapped to the mouse reference genome (mm10) using HISAT2. Peak calling of hydroxymethylated regions was carried out using MACS2 with a q-value $<10^{-4}$. Differential hydroxymethylated regions (DhMRs) between groups were identified using diffReps ($\log_2$FC ≥ 1, $P \leq 10^{-4}$). Peaks were annotated to the nearest transcription start site using the UCSC RefSeq database. Signal tracks (.bw files) were generated for visualization in IGV genome browser.

2.27. Chromatin immunoprecipitation and sequencing (ChIP-seq)

Chromatin immunoprecipitation sequencing was performed on primary mouse bone marrow-derived macrophages to assess histone modifications using antibodies against H3K4me3 (Cell Signaling Technology, Danvers, MA, USA; #5326 and #9751). Cells were crosslinked with 1% formaldehyde for 10 min at room temperature and quenched with 0.125 mol/L glycine. Chromatin was extracted and sheared by sonication to 200−500 bp fragments. Immunoprecipitation was carried out overnight at 4 °C with 5 μg of antibody and protein A/G magnetic beads. After elution and reversal of crosslinks, DNA was purified and used for library construction with the NEBNext Ultra II DNA Library Prep Kit (New England Biolabs, Ipswich, MA, USA). Libraries were quality-checked using an Agilent 2100 Bioanalyzer (Agilent Technologies, Santa Clara, CA, USA) and sequenced on NovaSeq 6000 platform (Illumina, San Diego, CA, USA) (paired-end, 150 bp). Raw reads were saved in FASTQ format. Sequencing quality was assessed using Fastp (v0.23.1), and key metrics including read number, total bases, GC content, Q20/Q30 base percentages, and sequencing error rates were computed and visualized in R. Clean reads were aligned to the mouse genome (mm39) using Bowtie.

2.28. RNA sequencing and data analysis

Total RNA was extracted from left ventricular tissues of mice in each group and assessed for quality *via* 1% agarose gel electrophoresis. RNA purity and integrity were measured using a NanoPhotometer (Implen, Munich, Germany) and Agilent 2100 Bioanalyzer (Agilent Technologies, Santa Clara, USA) with the RNA Nano 6000 Kit (Agilent Technologies). For library preparation, 1 μg RNA per sample was processed using the NEBNext Ultra RNA Library Prep Kit (New England Biolabs, Ipswich, USA), with size selection (250−300 bp) *via* AMPure XP beads (Beckman Coulter, Brea, USA), followed by PCR amplification and quality checks. Clustering and sequencing were performed on a cBot Cluster Generation System (Illumina, San Diego, USA)

Figure 2 Hematopoietic *Tet2*$^{+/-}$ clonal expansion accelerates with age and aggravates cardiac aging phenotypes. (A) Single-cell RNA-seq of CD45$^+$ cells identified 10 immune subtypes. (B, C) SASP-related genes (*Spp1*, *S100a8*, *S100a9*) and inflammatory cytokines (*Il1b*, *Tnf*, *Il1a*) were upregulated in monocytes/macrophages in *Tet2*-KO mice. (D) Schematic of BMT. CD45.2$^+$ *Tet2*$^{+/+}$ ($n = 6$) or *Tet2*$^{+/-}$ bone marrow cells were transplanted into CD45.1 recipients; myeloid cells were monitored from 0 to 13 months post-transplantation. Expansion rates of CD45$^+$ cells (E), monocytes/macrophages (F), and neutrophils (G) over time. Representative images and quantification of myocardial fibrosis (Masson's trichrome, H) and collagen I immunofluorescence (I), scale bars, 50 μm. (J) Transmission electron microscopy analysis of BMT-mice hearts. Left: representative images (orange arrows, Z-disc; white dashed lines, sarcomere length). Right: the sarcomere length is quantified. Scale bar: 500 nm. RT-qPCR analysis of Bnp (K) and Anp (L) transcript levels in heart tissue. (M) Western blot of P21 protein in heart tissue. Immunohistochemistry for P21 (N), IL1B (O), TNFA (P), S100A8 (Q), and S100A9 (R). Quantification of P21, S100A8, and S100A9 is shown as percentage of positive cells; IL1B and TNFα are shown as percentage of positive area, scale bars, 20 μm $^{**}P < 0.01$, Statistical significance was determined by Mann−Whitney U test (H−R). Data are presented as mean ± SEM; $n = 6$ biological replicates. SASP, Senescence-associated secretory phenotype; BMT, bone marrow transplantation. Anp/Bnp, atrial/brain natriuretic peptide.

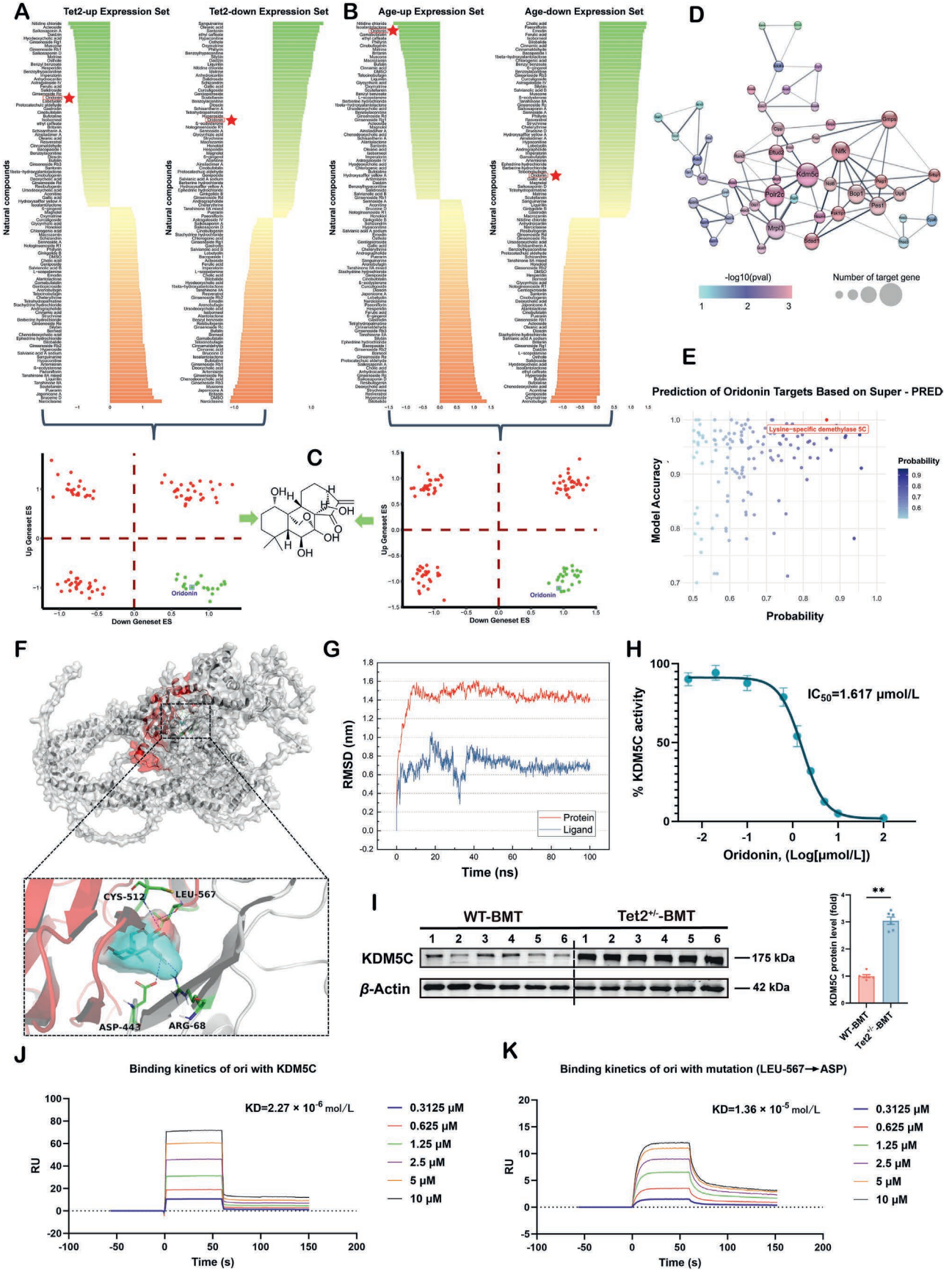
A
Tet2-up Expression Set
Tet2-down Expression Set
Natural compounds
B
Age-up Expression Set
Age-down Expression Set
Natural compounds
C
Up Geneset ES
Down Geneset ES
Oridonin
D
-log10(pval)
Number of target gene
E
Prediction of Oridonin Targets Based on Super - PRED
Lysine−specific demethylase 5C
Model Accuracy
Probability
F
CYS-512
LEU-567
ASP-443
ARG-68
G
RMSD (nm)
Time (ns)
Protein
Ligand
H
% KDM5C activity
IC50=1.617 μmol/L
Oridonin, (Log[μmol/L])
I
WT-BMT
Tet2+/--BMT
KDM5C
β-Actin
175 kDa
42 kDa
KDM5C protein level (fold)
J
Binding kinetics of ori with KDM5C
KD=2.27 × 10-6 mol/L
RU
Time (s)
0.3125 μM
0.625 μM
1.25 μM
2.5 μM
5 μM
10 μM
K
Binding kinetics of ori with mutation (LEU-567→ASP)
KD=1.36 × 10-5 mol/L
RU
Time (s)
0.3125 μM
0.625 μM
1.25 μM
2.5 μM
5 μM
10 μM

and NovaSeq 6000 platform (Illumina) to generate 150 bp paired-end reads. Raw FASTQ reads were filtered with custom scripts to remove adapters, poly-Ns, and low-quality reads. Clean reads were evaluated for Q20, Q30, and GC content, and aligned to the mm10 mouse genome using Hisat2 (v2.0.5). Read counts were obtained, and differential expression analysis was conducted using DESeq2 (v1.16.1), applying a negative binomial model. Despite limited replicates, differential genes were identified using established pipelines and reproducible trends. *P*-values were adjusted using the Benjamini−Hochberg method (adjusted $P < 0.05$). PPI networks were constructed *via* STRING. GSEA was performed with the Broad GSEA tool using Hallmark and KEGG gene sets (MSigDB v7.5). Analyses and visualizations were completed in R.

2.29. Data and statistical analysis

Nonnormally distributed data were analyzed for statistical significance by Mann−Whitney U test. Statistical analysis was performed using one-way analysis of variance (ANOVA) for comparisons among multiple groups, followed by Tukey's *post hoc* test. Comparisons between two groups were assessed using two-tailed unpaired Student's *t*-test. Analyses were conducted using GraphPad Prism (GraphPad Software, San Diego, USA) or R software (R Foundation for Statistical Computing, Vienna, Austria). All error bars represent the standard error of the mean (SEM.), and statistical significance was defined as $P < 0.05$.

2.30. Data availability

Data supporting the findings of this study are available from the corresponding author upon reasonable request. The mRNA and ChIP sequencing data generated in this study have been deposited in the National Center for Biotechnology Information Gene Expression Omnibus database (accession numbers: GSE299167 and GSE299168). The hMeDIP sequencing data generated in this study also have been deposited in the China National Center for Bioinformation (CNCB, accession number: subCRA053467).

3. Results

3.1. TET2-driven CHIP exhibits a causal association with CVD and the aging process

Age and cardiovascular disease are the primary factors associated with CHIP[38]. To investigate causal relationships, we conducted two-sample MR using large-scale GWAS summary statistics (Fig. 1A). Genetic instruments for CHIP subtypes were derived from an exome-wide GWAS ($n = 454{,}803$, UK Biobank)[28], defining CHIP status by recurrent, protein-altering somatic mutations across 23 genes. Eight driver genes (*DNMT3A*, *TET2*, *ASXL1*, *PPM1D*, *TP53*, *JAK2*, *SRSF2*, and *SF3B1*) were selected for subtype-specific analyses based on mutation frequency and biological relevance[8]. Genome-wide significant variants were extracted for each subtype. Outcome data included GrimAge-based aging biomarkers ($n = 34{,}467$) and exome-wide CVD outcomes ($n = 386{,}107$)[29,30]. MR analysis revealed that *TET2* was the only gene showing a significant causal relationship with both aging and CVD ($P < 0.001$), exerting the strongest effect across all tested subtypes (Fig. 1B and C, Supporting Information Figs. S1 and S2). Instrument strength (F-statistics), heterogeneity (Cochran's Q), and pleiotropy tests (MR-Egger intercept and MR-PRESSO global test) showed no weak instrument bias or directional pleiotropy, supporting the robustness of the causal estimates. Full statistics are available in Supporting Information Table S3.

To investigate the transcriptomic features of CHIP in the heart, we constructed a CHIP signature using MCPcounter on myocardial RNA-seq data from GSE226642 (36 CHIP carriers *vs*. 36 non-carriers). This signature, enriched for monocyte/macrophage markers, was applied to GSE57338 ($n = 313$), comprising non-failing, idiopathic dilated cardiomyopathy, and ischemic cardiomyopathy samples. CHIP scores were significantly elevated in dilated cardiomyopathy and ischemic cardiomyopathy, indicating disease-associated immune infiltration (Fig. 1D−F), and the CHIP scores were more prominent among men (Supporting Information Fig. S3A). We further assessed the correlation of CHIP scores with clinical and molecular parameters. In peripheral blood transcriptomes from CVD patients (GSE181114), CHIP scores were showed a positive correlation with age (Fig. 1G). Elevated CHIP scores were also associated with increased myocardial expression of stress (NPPB), fibrosis (ACTA2), and inflammatory markers (IL6, IL1B) (Fig. S3B−S3E). Together, MR and transcriptomic findings suggest that *Tet2*-driven CHIP contributes to age-related cardiac disorder.

3.2. Hematopoietic $Tet2^{+/-}$ clonal expansion aggravates cardiac aging phenotypes

Given its robust association with cardiovascular disease, TET2 was selected for mechanistic investigation. Using scRNA-seq data

Figure 3 Identification of oridonin as a potential anti-aging compound targeting KDM5C. (A, B) Bar plots showing enrichment scores of natural compounds based on their ability to reverse *Tet2*-deficient (A) and aging-associated (B) transcriptional signatures. Oridonin ranked among the top hits in both upregulated and downregulated gene sets. (C) Scatter plots displaying the distribution of enrichment scores across four gene sets; oridonin clusters in the bottom-right quadrant, indicating consistent gene expression reversal across all comparisons. (D) Protein−protein interaction network constructed from the top 50 oridonin-downregulated genes. Node size reflects the number of target genes; node color represents *P*-value significance. KDM5C appears as a prominent hub. (E) Super-PRED output showing predicted oridonin targets based on structural similarity; *x*-axis shows binding probability, *y*-axis indicates model accuracy. KDM5C is highlighted as a high-confidence hit. (F) Docking model of oridonin binding to the JmjC catalytic domain of KDM5C. Inset shows interaction with residues CYS512, LEU567, ASP443, and ARG68 at the binding pocket. (G) Molecular dynamics simulation over 100 ns showing RMSD trajectories for KDM5C protein (red) and oridonin ligand (blue), indicating stable binding conformation. (H) Dose−response curve of KDM5C enzymatic inhibition by oridonin *in vitro*. Data represent mean ± SEM; (I) Western blot showing increased KDM5C protein expression in $Tet2^{+/-}$BMT mice BMDM compared to WT. Quantification shown on the right. (J) Surface plasmon resonance (SPR) sensor gram depicting oridonin binding to recombinant KDM5C at increasing concentrations. (K) SPR assay with LEU567 to ASP mutant shows reduced binding, supporting the functional relevance of the predicted docking site. BMT, bone marrow transplantation. Ori, oridonin. M, mol/L.

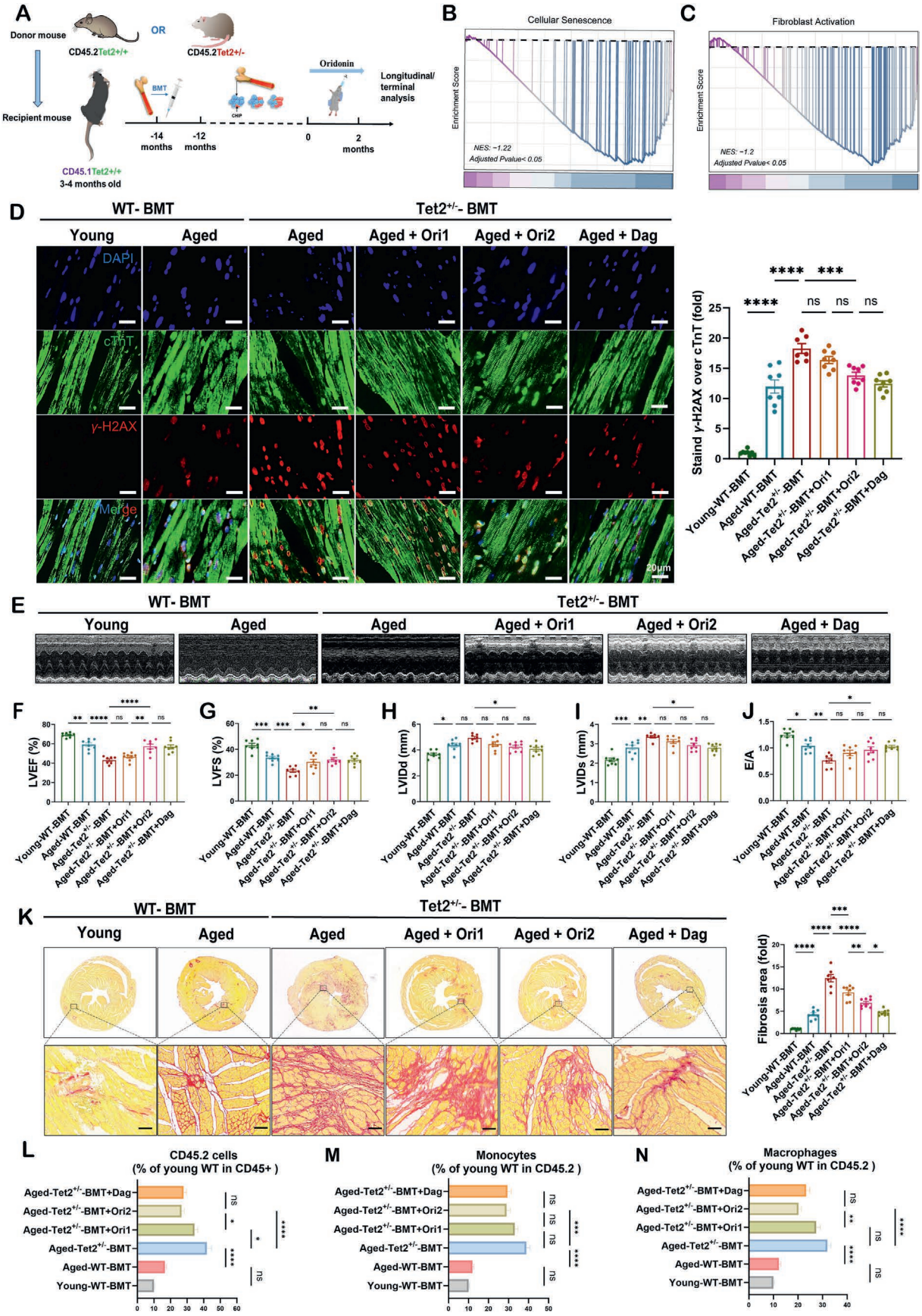
A
Donor mouse
CD45.2Tet2+/+
OR
CD45.2Tet2+/-
Recipient mouse
CD45.1Tet2+/+
3-4 months old
BMT
CHIP
Oridonin
-14 months
-12 months
0
2 months
Longitudinal/ terminal analysis
B
Cellular Senescence
Enrichment Score
NES: -1.22
Adjusted Pvalue< 0.05
C
Fibroblast Activation
Enrichment Score
NES: -1.2
Adjusted Pvalue< 0.05
D
WT- BMT
Tet2+/- BMT
Young
Aged
Aged
Aged + Ori1
Aged + Ori2
Aged + Dag
DAPI
cTnT
γ-H2AX
Merge
20μm
Staind γ-H2AX over cTnT (fold)
Young-WT-BMT
Aged-WT-BMT
Aged-Tet2+/- -BMT
Aged-Tet2+/- -BMT+Ori1
Aged-Tet2+/- -BMT+Ori2
Aged-Tet2+/- -BMT+Dag
E
WT- BMT
Tet2+/- BMT
Young
Aged
Aged
Aged + Ori1
Aged + Ori2
Aged + Dag
F
LVEF (%)
G
LVFS (%)
H
LVIDd (mm)
I
LVIDs (mm)
J
E/A
K
WT- BMT
Tet2+/- BMT
Young
Aged
Aged
Aged + Ori1
Aged + Ori2
Aged + Dag
Fibrosis area (fold)
L
CD45.2 cells
(% of young WT in CD45+)
M
Monocytes
(% of young WT in CD45.2)
N
Macrophages
(% of young WT in CD45.2)
Aged-Tet2+/-BMT+Dag
Aged-Tet2+/-BMT+Ori2
Aged-Tet2+/-BMT+Ori1
Aged-Tet2+/-BMT
Aged-WT-BMT
Young-WT-BMT

(GSE225773) from CHIP model mice, ten immune cell types within CD45$^+$ populations were identified *via* SingleR annotation (Fig. 2A). In macrophages and monocytes, aging-associated SASP genes (*Spp1*, *S100a8*, *S100a9*) and inflammatory cytokines (*Il1b*, *Tnf*, *Il1a*) were markedly upregulated in *Tet2-KO* compared to WT (Fig. 2B and C), suggesting an inflammatory transcriptional reprogramming in myeloid cells derived from CHIP clones. Cell cycle analysis revealed *Tet2-KO* monocytes/macrophages displayed a significant reduction in G1 phase cells and increase in S phase cells (Supporting Information Fig. S4A and S4B), indicating enhanced proliferative activity.

To validate the causal role of hematopoietic *Tet2*$^{+/-}$ expansion in cardiac aging, we established a competitive bone marrow transplantation model according to previous studies[19,36]. CD45.2$^+$ *Tet2*$^{+/+}$or *Tet2*$^{+/-}$ bone marrow cells were transferred into young CD45.1$^+$ recipients, after 2 months followed by 12 months long-term tracking (Fig. 2D). *Tet2*$^{+/-}$ clones exhibited comparable expansion to WT in early stages but expanded significantly faster from 8 months onward (Fig. 2E), particularly within monocyte/macrophage and neutrophil compartments (Fig. 2F and G, Supporting Information Fig. S5). Further analyses revealed that macrophages derived from *Tet2*$^{+/-}$ hematopoietic clones displayed enhanced SASP factor secretion, which in turn promoted cardiomyocyte senescence-related transcriptional responses in a paracrine manner (Supporting Information Figs. S6 and S7). Histological analysis of aged hearts revealed increased myocardial fibrosis (Fig. 2H) and collagen deposition (Fig. 2I) in *Tet2*$^{+/-}$-BMT mice. Transmission electron microscopy showed sarcomere disarray and elongation (Fig. 2J), suggesting structural degeneration of cardiomyocytes. Expression of cardiac stress markers Atrial/Brain natriuretic peptide (ANP/BNP) was also elevated (Fig. 2K and L). At the molecular level, p21 expression was markedly increased in *Tet2*$^{+/-}$BMT hearts (Fig. 2M and N). To further validate the senescent phenotype, P16 and P53 were also examined and found to be upregulated, while SABGALactosidase staining confirmed increased senescent cardiomyocytes compared with WT-BMT controls (Supporting Information Fig. S8). These results indicate that hematopoietic TET2 deficiency accelerates cardiac senescence. In parallel, SASP-related genes (*Il1b*, *Tnf*, *S100a8*, *S100a9*) were elevated (Fig. 2O−R), consistent with a pro-inflammatory aging phenotype previously linked to CHIP-related cardiovascular risk[39].

In summary, these data demonstrate that *Tet2*$^{+/-}$ drives age-progressive hematopoietic clonal expansion, which in turn promotes cardiac inflammation, fibrosis, and structural deterioration. The *Tet2*$^{+/-}$BMT model provides functional evidence that CHIP exacerbates physiological cardiac aging through myeloid-biased expansion and SASP-associated inflammation.

3.3. Transcriptome-guided identification of oridonin as a potential anti-aging compound targeting KDM5C

To identify natural compounds with potential therapeutic effects on aging, we conducted a transcriptome-based screening strategy according our previous studies[31-35], using four gene sets: upregulated and downregulated genes associated with both *Tet2*-deficient CHIP and aging-related signatures. Using our previously established transcriptomic library of 152 natural small molecules, we calculated enrichment scores for each compound in relation to these four gene sets. Compounds that simultaneously reversed the upregulated genes and restored the downregulated genes in both *Tet2*$^{-/-}$and aging contexts were considered potential anti-aging candidates (Fig. 3A and B). Among them, oridonin, a bioactive diterpenoid, showed consistent and significant reversal of aging- and CHIP-associated gene expression patterns across all four sets (Fig. 3C). To validate the functional effects of the candidate compound identified from transcriptomic screening, oridonin (4 μmol/L, 24 h) treatment significantly reduced the mRNA expression of SASP-related genes, including *Il6*, *Il1b*, *Tnf* and *Ccl2* (Supporting Information Fig. S9A−S9D), in *Tet2*$^{+/-}$ BMDMs was applied based on CCK-8 viability testing. To further explore the potential molecular targets of oridonin, we performed a protein−protein interaction (PPI) network analysis based on the top 50 downregulated genes identified from the oridonin-induced transcriptome profile. The PPI network revealed several interconnected nodes, with Kdm5c emerging as one of the central hubs (Fig. 3D). To further validate the potential interaction between oridonin and *Kdm5c*, we applied the Super-PRED platform[40] to predict possible molecular targets of oridonin based on chemical structure similarity and pharmacophore matching. The analysis revealed that *Kdm5c* ranked among the top predicted targets, with high model accuracy and binding probability (Probability >0.9; Accuracy = 1.0, Fig. 3E).

To further investigate the potential interaction between oridonin and KDM5C, we conducted molecular docking and molecular dynamics simulations. Molecular docking revealed that oridonin binds to the JmjC domain of KDM5C, a catalytically essential region responsible for demethylase activity. The docking pose showed that oridonin forms stable interactions with key residues including CYS512, LEU567, ASP443, and ARG68

Figure 4 Oridonin treatment mitigates cardiac aging and dysfunction in aged *Tet2*$^{+/-}$ BMT mice *in vivo* and reduces clonal hematopoietic expansion. (A) Experimental design. After BMT in 3−4 months mice, animals were observed for 12 months before receiving oridonin treatment for 2 months. GSEA plot shows cellular senescence-associated (B) differentially expressed genes (DEGs) and fibroblast activation-related DEGs (C) in heart of aged *Tet2*$^{+/-}$ mice after oridonin treatment. (D) Immunofluorescence staining of heart sections from BMT mice shows the colocalization (yellow) of γH2AX (red) and cTnT (green, cardiomyocyte-specific). Left: representative images (scale bar = 20 μm); Right: quantification of γH2AX/cTnT colocalization. (E) Representative echocardiographic images of BMT mice. Echocardiographic parameters include: (F) left ventricular ejection fraction (LVEF), (G) fractional shortening (LVFS), (H) left ventricular internal diameter at diastole (LVIDd), (I) at systole (LVIDs), and (J) the E/A ratio (peak early diastolic to late atrial filling velocity). (K) Sirius red staining of BMT mouse hearts. Left: representative images (scale bar = 50 μm); Right: quantification of fibrotic area. Flow cytometric quantification of CD45.2$^+$ leukocytes (L), monocytes (M), and macrophages (N) in myeloid cells of BMT mice. Data are presented as mean ± SEM. *$P < 0.05$, **$P < 0.01$, ***$P < 0.001$, and ****$P < 0.0001$ by one-way ANOVA with Tukey's *post hoc* test ($n = 7$−8 mice per group). NES, normalized enrichment score; BMT, bone marrow transplantation; Ori1, oridonin-treated 20 mg/kg; Ori2, oridonin-treated 40 mg/kg; Dag, dapagliflozin. ns, not significant.

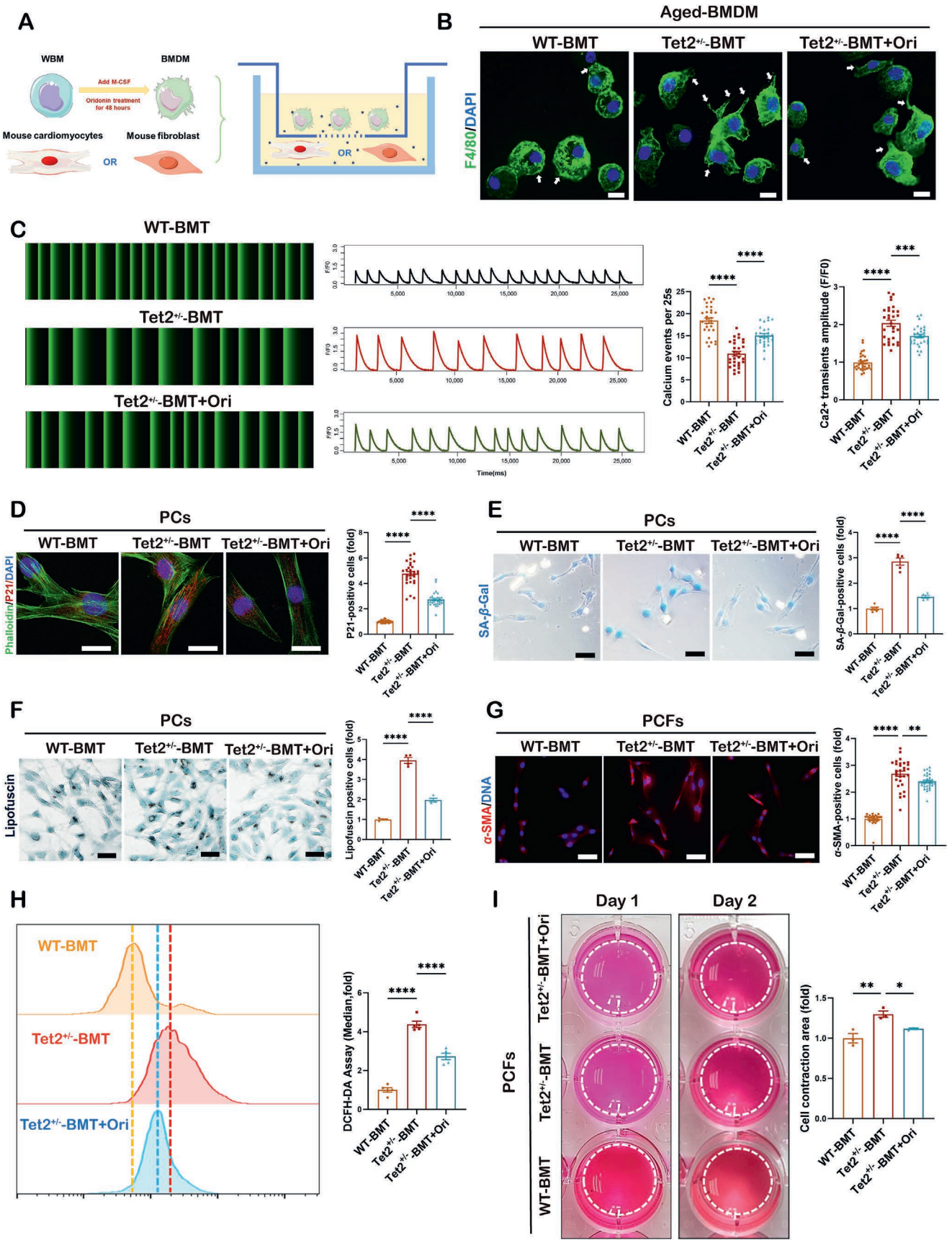

Figure 5 Cellular co-culture models reveal that oridonin directly alleviates *Tet2*$^{+/-}$ induced cardiac aging phenotypes *in vitro*. (A) Co-culture experimental design: PCs or PCFs were co-cultured with BMDMs from aged BMT mice, with or without oridonin treatment. (B) Representative

(Fig. 3F). Subsequent 100 ns Molecular dynamics simulations demonstrated that the ligand−protein complex remains stable over time, with the RMSD of the ligand fluctuating below 0.8 nm (Fig. 3G), oridonin stabilizes KDM5C through enhanced compactness, reduced solvent exposure, and key hydrophobic and electrostatic interactions, supporting a stable and energetically favorable binding conformation (Supporting Information Fig. S10A−S10G). To experimentally validate the inhibitory effect of oridonin on KDM5C enzymatic activity, we conducted an *in vitro* activity assay. Oridonin exhibited a dose-dependent suppression of KDM5C activity (Fig. 3H). The same assay was performed for KDM5A/B/D. These isoforms showed demethylase activity as well, and the activity trend was consistent with KDM5C (Supporting Information Fig. S11). Furthermore, Western blot analysis revealed a significant upregulation of KDM5C protein levels in *Tet2*$^{+/-}$–BMT compared to WT-BMT controls, suggesting that TET2 insufficiency leads to KDM5C overexpression (Fig. 3I). To validate the direct physical interaction between oridonin and KDM5C, we performed surface plasmon resonance assays. Oridonin binds to recombinant KDM5C protein with high affinity (Fig. 3J). Consistent with this notion, inhibition of NFκB signaling markedly reduced KDM5C protein levels in BMDMs derived from *Tet2*$^{+/-}$BMT mice (Supporting Information Fig. S12), suggesting that KDM5C upregulation is at least partially driven by SASP-associated inflammatory activation. To assess whether this binding is dependent on the predicted docking residue LEU567, we introduced a point mutation (LEU567 to ASP) within the JmjC domain of KDM5C and repeated the SPR analysis. The mutation significantly reduced the binding response units across all tested oridonin concentrations (Fig. 3K). Collectively, oridonin may serve as a potential therapeutic agent against cardiac aging, with KDM5C being a putative downstream target.

3.4. Oridonin effectively inhibits cardiac aging driven by Tet2$^{+/-}$ *in aged CHIP mice and reduces the expansion of hematopoietic stem cells*

To evaluate the therapeutic efficacy of oridonin in attenuating *Tet2*$^{+/-}$driven cardiac aging, a BMT model was established in young mice (3−4 months), followed by 12 months of aging and 2 months of intervention with oridonin or the positive control dapagliflozin (Fig. 4A). To evaluate the *in vivo* safety of oridonin, we performed serum biochemical analyses using ELISA kits for ALT, AST, BUN, and creatinine. No significant differences were observed among *Tet2*$^{+/-}$BMT aged, dapagliflozin and oridonin 20 mg/kg (ori1) and 40 mg/kg(ori2) groups. Histological evaluation of liver and kidney by H&E staining revealed preserved tissue architecture without overt necrosis Only mild, non-specific age-related changes were observed (Supporting Information Fig. S13). These results indicate that oridonin was well tolerated at the doses tested. Transcriptomic analysis revealed that oridonin significantly downregulated gene signatures related to cellular senescence and fibroblast activation in *Tet2*$^{+/-}$BMT hearts (Fig. 4B and C). Downregulation of fibrosis-related genes (*Col1a1*, *Col1a2*, *Vim*, *Twist1*) and SASP mediators (*Tnf*, *S100a8/a9*, *Il6*) further supported the anti-senescent and anti-fibrotic effect of oridonin (Supporting Information Fig. S14A), consistent with reversal of the pathological gene expression profile (Fig. S14B and S14C). To assess cellular senescence, γH2AX was co-stained with cTnT in heart tissue. Compared to young controls, aged WT-BMT mice showed increased γH2AX cardiomyocytes, which were further elevated in aged *Tet2*$^{+/-}$BMT mice. Oridonin significantly reduced γH2AX positivity, comparable to dapagliflozin (Fig. 4D). Cardiac function was evaluated by transthoracic echocardiography. Aged *Tet2*$^{+/-}$BMT mice exhibited reduced LVEF, LVFS, and the E/A ratio, along with increased LVIDd, and LVIDs compared to young or aged WT-BMT mice. Oridonin treatment improved both systolic and diastolic function in a dose-dependent manner, with oridonin treatment achieving similar efficacy to dapagliflozin (Fig. 4E−J). Histological analysis using Sirius red staining showed enhanced myocardial fibrosis in aged WT-BMT mice and more severe fibrosis in *Tet2*$^{+/-}$BMT mice. Both doses of oridonin significantly reduced fibrosis, with high-dose oridonin comparable to dapagliflozin (Fig. 4K). Finally, we assessed the effect of oridonin on clonal hematopoiesis. Aged *Tet2*$^{+/-}$BMT mice exhibited elevated frequencies of CD45.2^{+} leukocytes, particularly monocytes and macrophages, compared to WT controls. Macrophages were selectively further quantified given their central role in driving age-associated cardiac remodeling and dysfunction[41,42]. Oridonin treatment significantly reduced the abundance of monocytes and macrophages in a dose-dependent manner, with achieving reductions comparable to those observed with dapagliflozin (Fig. 4L−N). Notably, these changes were not observed in aged WT-BMT mice, suggesting a *Tet2*-dependent mechanism.

Altogether, these results demonstrate that oridonin effectively attenuates *Tet2*$^{+/-}$induced cardiac aging, fibrosis, and clonal hematopoietic expansion in a CHIP mouse model. The therapeutic effects were dose-dependent and comparable to those of dapagliflozin, supporting oridonin's potential as a targeted intervention for CHIP-associated cardiovascular aging.

images showing F4/80-labeled primary BMDMs from aged BMT mice displaying prominent filopodia. Scale bar, 20 μm. (C) Representative calcium recordings (left) of mouse PCs after co-culture with BMDMs. Right: quantification of calcium event frequency and calcium transient amplitude ($n = 30$ cells). (D) Representative images (left) and quantification (right) of P21 (red) and phalloidin (green) staining in mouse PCs ($n = 30$ cells). P21 expression levels were calculated as the mean fluorescence intensity using automated, unbiased quantification. Scale bar, 15 μm. (E) Representative images (left) and quantification (right) of SA-β-Gal staining in mouse PCs ($n = 100$ cells from five independent experiments). Scale bar, 50 μm. (F) Representative images (left) and quantification (right) of lipofuscin deposition in mouse PCs, evaluated using the Schmorl iron reduction method ($n = 100$ cells from four independent experiments). Scale bar, 50 μm. (G) Representative images (left) and quantification (right) of α-SMA (red) expression in mouse PCFs ($n = 30$ cells). Scale bar, 50 μm. (H) Reactive oxygen species (ROS) generation in mouse PCs was analyzed by flow cytometry using DCFH-FA staining. Right: median ROS levels were quantified ($n = 5$ samples per group). (I) Representative images (left) and quantification (right) of collagen lattice contraction by PCFs ($n = 3$ samples per group). Data are shown as mean ± SEM. $^{*}P < 0.05$, $^{**}P < 0.01$, $^{***}P < 0.001$, and $^{****}P < 0.0001$ by one-way ANOVA with Tukey's *post hoc* test (panels C−I). Abbreviations: WBM, whole bone marrow; BMDM, bone marrow-derived macrophages; PCs, primary cardiomyocytes; PCFs, primary cardiac fibroblasts; Ori, oridonin; BMT, bone marrow transplantation.

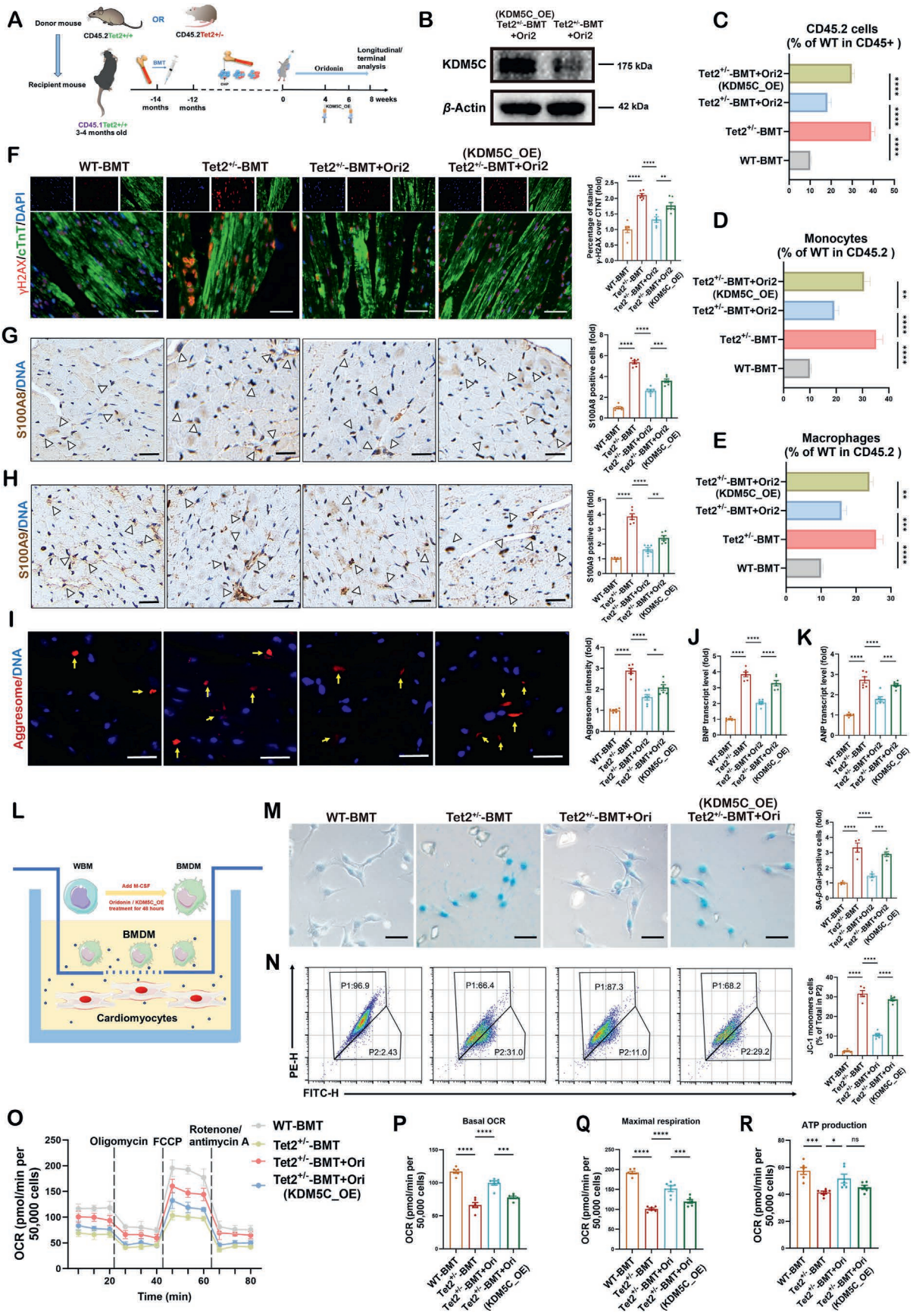
A
Donor mouse
CD45.2Tet2+/+
OR
CD45.2Tet2+/-
Recipient mouse
CD45.1Tet2+/+
3-4 months old
BMT
-14 months
-12 months
0
4
6
8 weeks
Oridonin
Longitudinal/ terminal analysis
KDM5C_OE
B
(KDM5C_OE) Tet2+/--BMT +Ori2
Tet2+/--BMT +Ori2
KDM5C
175 kDa
β-Actin
42 kDa
C
CD45.2 cells (% of WT in CD45+)
Tet2+/--BMT+Ori2 (KDM5C_OE)
Tet2+/--BMT+Ori2
Tet2+/--BMT
WT-BMT
D
Monocytes (% of WT in CD45.2)
E
Macrophages (% of WT in CD45.2)
F
WT-BMT
Tet2+/--BMT
Tet2+/--BMT+Ori2
(KDM5C_OE) Tet2+/--BMT+Ori2
γH2AX/cTnT/DAPI
Percentage of staind γ-H2AX over CTNT (fold)
G
S100A8/DNA
S100A8 positive cells (fold)
H
S100A9/DNA
S100A9 positive cells (fold)
I
Aggresome/DNA
Aggresome intensity (fold)
J
BNP transcript level (fold)
K
ANP transcript level (fold)
L
WBM
BMDM
Add M-CSF
Oridonin / KDM5C_OE treatment for 48 hours
BMDM
Cardiomyocytes
M
WT-BMT
Tet2+/--BMT
Tet2+/--BMT+Ori
(KDM5C_OE) Tet2+/--BMT+Ori
SA-β-Gal-positive cells (fold)
N
P1:96.9
P2:2.43
P1:66.4
P2:31.0
P1:87.3
P2:11.0
P1:68.2
P2:29.2
PE-H
FITC-H
JC-1 monomers cells (% of Total in P2)
O
Oligomycin
FCCP
Rotenone/ antimycin A
WT-BMT
Tet2+/--BMT
Tet2+/--BMT+Ori
Tet2+/--BMT+Ori (KDM5C_OE)
OCR (pmol/min per 50,000 cells)
Time (min)
P
Basal OCR
Q
Maximal respiration
R
ATP production

3.5. Oridonin attenuates cardiomyocyte aging by modulating macrophage dysfunction in an in vitro Tet2-mutation CHIP model

To further assess the mechanistic role of oridonin in mitigating *Tet2* mutation-induced cardiac aging, we established a Transwell-based co-culture system (Fig. 5A). According to the previous research[34,43], BMDMs were isolated from aged BMT mice, while PCs and PCFs were harvested from 8-week-old wild-type mice. Oridonin (4 μmol/L, 48 h) was applied based on CCK-8 viability testing (Supporting Information Fig. S15), which confirmed minimal cytotoxicity at this concentration. F4/80 staining showed that oridonin reduced the senescence-associated pseudopodia in *Tet2*$^{+/-}$BMT-derived macrophages (Fig. 5B). Functional impairments in cardiomyocytes were assessed *via* calcium imaging. PCs co-cultured with *Tet2*$^{+/-}$BMT BMDMs showed reduced calcium transient frequency and elevated amplitude, consistent with dysregulated excitation−contraction coupling. These defects were less prominent in WT-BMT co-cultures and were significantly ameliorated following oridonin treatment (Fig. 5C). Molecular aging markers in PCs were also evaluated. Compared to WT-BMT controls, *Tet2*$^{+/-}$BMT co-cultured PCs exhibited elevated levels of P21, SA-β-Gal activity, lipofuscin accumulation, and oxidative DNA damage, all of which were significantly attenuated by oridonin (Fig. 5D−F and H). These results support that *Tet2*-driven macrophage dysfunction contributes to paracrine induction of cardiomyocyte senescence, which is reversible with oridonin. In parallel, aging phenotypes in PCFs were assessed. *Tet2*$^{+/-}$BMT co-culture induced upregulation of α-SMA, a myofibroblast activation marker, and impaired collagen gel contraction capacity, both of which were improved following oridonin treatment (Fig. 5G and I), indicating reduced fibroblast-to-myofibroblast transition and matrix stiffness regulation.

Collectively, these findings demonstrate that *Tet2* mutation-associated CHIP accelerates cardiac aging through macrophage-driven paracrine, and that oridonin mitigated this effect by suppressing macrophage-mediated SASP signaling, thereby restoring cardiomyocyte and fibroblast phenotype and function.

3.6. Oridonin counteracts CHIP-driven cardiac aging induced by Tet2 mutation through KDM5C inhibition

Building on transcriptomic profiling that identified KDM5C as a potential downstream effector of oridonin, we conducted *in vivo* mechanistic validation using AAV-mediated KDM5C overexpression (KDM5C_OE) in aged *Tet2*$^{+/-}$BMT mice treated with high-dose oridonin (Ori2), the most efficacious dose identified in previous experiments (Fig. 6A). Western blot analysis confirmed that KDM5C protein levels were significantly elevated following viral KDM5C overexpression in oridonin-treated mice (Fig. 6B). Oridonin treatment markedly reduced the proportions of CD45.2^{+} *Tet2*$^{+/-}$ leukocytes, monocytes, and macrophages in myeloid cells, which were reversed upon KDM5C_OE expression (Fig. 6C−E). In cardiac tissues, oridonin intervention attenuated DNA damage marker γH2AX fluorescence intensity (Fig. 6F), decreased S100A8 (Fig. 6G) and S100A9 (Fig. 6H) immunopositivity, and reduced protein aggregate accumulation (Fig. 6I). However, these aging-associated markers significantly rebounded following KDM5C_OE. Consistent trends were observed in the expression of BNP and ANP, indicative of cardiac dysfunction (Fig. 6J and K). These findings were further validated *in vitro*. BMDMs from aged BMT mice were co-cultured with primary cardiomyocytes and treated with oridonin, with or without KDM5C_OE (Fig. 6L). Oridonin reduced SA-β-Gal activity in co-cultured PCs, whereas KDM5C_OE reversed this effect (Fig. 6M). Additionally, KDM5C_OE after oridonin treatment led to decreased mitochondrial membrane potential (Fig. 6N) and impaired mitochondrial respiration, evidenced by reduced basal respiration, maximal respiration, and ATP production (Fig. 6O−R). Additionally, the comparable suppression of SASP genes by oridonin, the selective KDM5C inhibitor, and lentiviral *Kdm5c* knockdown in *Tet2*$^{+/-}$BMT BMDMs provides convergent functional evidence that KDM5C acts as a central mediator of *Tet2* deficiency−driven inflammatory and senescent phenotypes (Supporting Information Figs. S16 and S17).

Taken together, these findings establish KDM5C as a functional mediator of *Tet2* mutation-induced clonal hematopoiesis and cardiac aging. Oridonin's cardioprotective and anti-CHIP effects are at least partially dependent on KDM5C inhibition.

3.7. Oridonin induces H3K4me3 accumulation and promotes SIRT2/STAT-associated transcription of longevity-related genes

Given that KDM5C functions as a histone H3K4 demethylase, we next performed ChIP-seq assays targeting H3K4me1 and H3K4me3 to investigate its epigenetic effects. Our data showed that knockdown of *Kdm5c* had minimal impact on H3K4me1

Figure 6 Oridonin reduces the rate of clonal hematopoiesis and cardiac aging induced by *Tet2*$^{+/-}$ through inhibition of KDM5C. (A) Experimental design. (B) Western blot analysis of KDM5C expression in BMDMs from *Tet2*$^{+/-}$ BMT mice and after AAV-mediated KDM5C_OE. Longitudinal quantification of CD45.2-WT and CD45.2- *Tet2*$^{+/-}$ leukocytes (C), monocytes (D), and macrophages (E) in myeloid cells of BMT mice. (F) Immunofluorescence staining of heart sections from BMT mice to detect the colocalization (yellow) of γH2AX (red) and cTnT (green, cardiomyocyte-specific). Left: representative images (scale bar = 20 μm); Right: quantitative analysis of γH2AX/cTnT colocalization. (G, H) Immunohistochemical analysis of S100A8 (G) and S100A9 (H) expression in BMT mouse hearts. Left: representative images (scale bar = 20 μm); Right: quantification of the proportion of positively stained cells. (I) Immunofluorescence staining for aggresome in BMT mouse hearts. Left: representative images (scale bar = 20 μm); Right: quantification of relative intensity. RT-qPCR analysis of Bnp (J) and Anp (K) expression in BMT mouse hearts. (L) Co-culture experimental design: BMDMs from BMT mice were co-cultured with PCs and treated with oridonin and/or AAV-mediated KDM5C_OE. (M) Representative images (left) and quantification (right) of SA-β-Gal staining in mouse PCs (n = 100 cells from four independent experiments). (N) Mitochondrial membrane potential in PCs was analyzed by flow cytometry using JC-1 staining. Right: quantification of the proportion of JC-1 monomer cells (n = 5 independent experiments). (O) Mitochondrial respiration analysis of mouse PCs using the Seahorse platform. (P−R) Quantification of basal oxygen consumption rate (OCR), maximal respiration, and ATP production. Data are shown as mean ± SEM. *$P < 0.05$, **$P < 0.01$, ***$P < 0.001$, and ****$P < 0.0001$ by one-way ANOVA with Tukey's *post hoc* test (n = 6 mice per group). Abbreviations: WBM, whole bone marrow; BMDM, bone marrow-derived macrophages; PCs, primary cardiomyocytes; PCFs, primary cardiac fibroblasts; Ori, oridonin; BMT, bone marrow transplantation. AAV, adeno-associated virus; KDM5C_OE, KDM5C overexpression; ns, not significant.

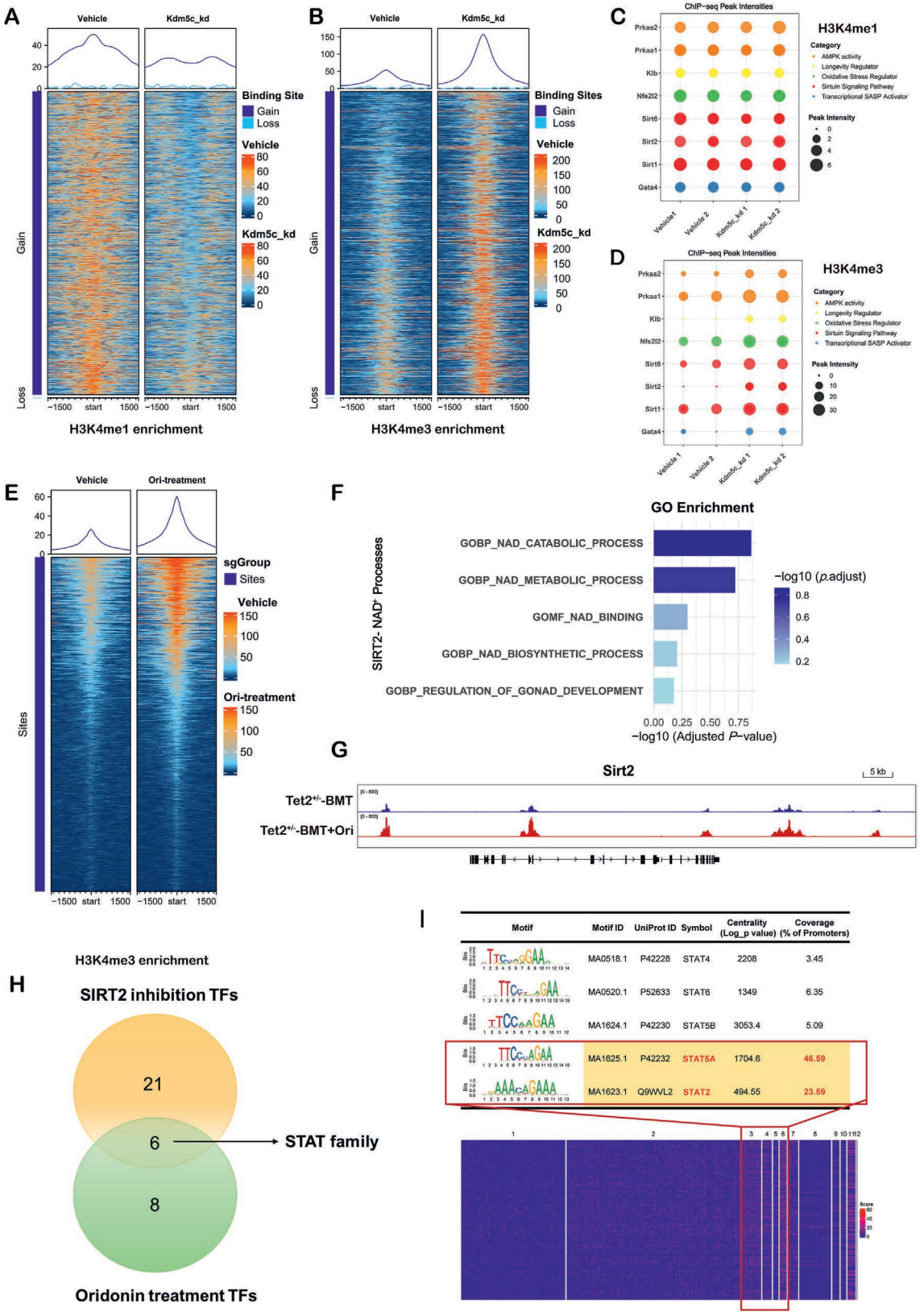

Figure 7 Epigenetic modulation of H3K4me3 by oridonin and its potential regulation *via* STAT family transcription factors. (A, B) Heatmaps and profile plots of H3K4me1 and H3K4me3 ChIP-seq signals in Vehicle and Kdm5c knockdown (kd) samples. While H3K4me1 levels remain largely unchanged (A), H3K4me3 signals are substantially elevated at gain regions in the *Kdm5c*_kd group (B). (C, D) Dot plots displaying ChIP-seq peak intensities at selected promoters of genes involved in AMPK signaling, oxidative stress response, and longevity regulation. (E) Genome-

levels across genomic regions (Fig. 7A). In contrast, H3K4me3 signals exhibited a marked increase upon *Kdm5c* knockdown, indicating that KDM5C predominantly regulates the trimethylated form of H3K4 (Fig. 7B). Additionally, we characterized the genomic distribution of differential H3K4me1 and H3K4me3 peaks. Further analysis showed that H3K4me3 peaks were highly enriched at promoter regions and exhibited greater fold-change than H3K4me1 (Supporting Information Fig. S18A−S18D).

To explore the functional relevance of these epigenetic alterations, we analyzed ChIP-seq enrichment at the promoter regions of several key genes involved in anti-aging, oxidative stress resistance, and longevity pathways, including *Sirt1/2/6*, *Nfe2l2*, *Klb*, and *Prkaa1/2*. The results revealed no significant changes in H3K4me1 enrichment, but a consistent upregulation of H3K4me3 at these loci, particularly in genes associated with AMPK signaling, Sirtuin pathways, and oxidative stress regulation (Fig. 7C and D). We next examined whether oridonin treatment recapitulates the epigenetic effects of *Kdm5c* knockdown. ChIP-seq profiling of H3K4me3 revealed a substantial global increase in trimethylation levels upon oridonin administration, similar to the effect observed in *Kdm5c*-deficient cells (Fig. 7E). Functional enrichment analysis of genes exhibiting oridonin-induced H3K4me3 upregulation revealed a significant enrichment of NAD^+ metabolic and catabolic processes, which are intimately associated with SIRT2-mediated regulation of aging, energy homeostasis, and chromatin dynamics[44] (Fig. 7F). Among these, *Sirt2*, a known regulator of longevity and oxidative stress, emerged as a key target. ChIP-seq signal visualization confirmed a marked increase in H3K4me3 enrichment at the *Sirt2* promoter in *Tet2*$^{+/-}$BMT mice after oridonin treatment (Fig. 7G). The enrichment of other potential targets, such as *Prkaa1/2*, *Klb*, *Nfe2l2*, *Sirt1/6*, and *Gata4* were weaker compared to *Sirt2* (Supporting Information Fig. S19). Given that H3K4me3 is associated with active transcription, this finding suggests that oridonin may promote *Sirt2* expression through epigenetic activation. To further elucidate the transcriptional mechanisms downstream of the SIRT2, we analyzed the transcriptomes of both SIRT2-inhibited and oridonin-treated samples. Enrichment analysis revealed a shared activation of STAT family transcription factors, which are well-established downstream effectors of SIRT2 and play a canonical role in regulating anti-aging pathways[45] (Fig. 7H). To test this, we performed motif enrichment analysis on H3K4me3-enriched promoter regions identified in oridonin ChIP-seq datasets, and found that clusters 3−7 highly enriched for pro-longevity and oxidative stress resistance genes. Motif analysis revealed that STAT5A and STAT2 binding motifs were prominently enriched across these clusters, covering 46.59% and 23.59% of promoters, respectively (Fig. 7I), suggesting that they may act as downstream mediators of the oridonin−KDM5C−SIRT2 axis, coordinating the transcriptional activation of anti-aging gene networks.

In summary, oridonin promotes H3K4me3-dependent activation of longevity pathways, potentially through the epigenetic activation of SIRT2-STAT-driven transcriptional programs.

3.8. Oridonin suppresses KDM5C to activate the SIRT2 anti-aging pathway and alleviate Tet2-driven CHIP-induced cardiac aging

Previous analysis revealed SIRT2 as a potential downstream effector of oridonin *via* H3K4me3 enrichment. Transcriptome data from *Tet2*$^{+/-}$BMT mouse hearts showed significant upregulation of *Sirt2* after oridonin treatment (Fig. 8A). To confirm its relevance, GSEA of public dataset GSE248894 revealed that *Sirt1/2* inhibition led to enrichment of aging-related gene sets and suppression of mitochondrial function pathways (Fig. 8B and C), supporting its central role in aging regulation. To validate the SIRT2-mediated anti-aging effect of oridonin, we introduced a SIRT2-specific inhibitor in the established BMDMs−cardiomyocyte co-culture model (Fig. 8D). Oridonin reduced SASP-related transcripts (*S100a8*, *S100a9*, *Tnf*, *Il6*, *Cdkn1a*, *Ccl2*), while SIRT2 inhibition partially reversed this effect (Fig. 8E). Phenotypically, oridonin decreased P21 expression, SA-β-Gal activity, and lipofuscin accumulation (Fig. 8F−H), improved mitochondrial membrane potential (Fig. 8J), and enhanced respiratory capacity reflected by elevated basal and maximal OCR and ATP output (Fig. 8K−N). SIRT2 blockade abolished these benefits. Similarly, in co-cultured cardiac fibroblasts, oridonin reduced α-SMA expression, a marker of fibrotic activation, which was reversed by SIRT2 inhibition (Fig. 8I).

Together, these results identify SIRT2 as a key mediator of oridonin's anti-CHIP effects, linking to mitochondrial and senescence regulation in *Tet2*-driven cardiac aging.

3.9. Oridonin protects against Tet2-CHIP cardiac aging via S100A8 suppression

To further identify key SASP effectors downstream of oridonin−SIRT2 suppression, we analyzed transcriptomic changes in SIRT2 inhibition and oridonin-treated *Tet2*$^{+/-}$BMT mice. Sankey mapping of inflammatory SASP factors confirmed *S100a8* is suppressed by oridonin, and this suppression is attenuated by SIRT2 inhibition (Fig. 9A). To assess its functional contribution, we administered recombinant S100A8 protein to oridonin-treated *Tet2*$^{+/-}$BMT mice (Fig. 9B). S100A8 reintroduction reversed oridonin-mediated reductions in BNP and ANP expression (Fig. 9C and D), and abolished its antifibrotic effects, as shown by Masson's trichrome staining and collagen I immunofluorescence (Fig. 9E and F). Echocardiography revealed that S100A8 treatment attenuated oridonin-induced improvements in cardiac function, including reductions in LVIDd/LVIDs and restoration of LVEF, LVFS, and E/A ratio (Fig. 9G−K). S100A8 gain-of-function also reactivated myocardial senescence. P21-positive nuclei increased in cardiomyocytes, indicating the re-emergence of DNA damage response and cell cycle arrest (Fig. 9L). In parallel, oridonin-suppressed proinflammatory cytokines *Il1b*, *Tnf*, *Ccl2*, and *Ccl5* were significantly upregulated after S100A8 administration (Fig. 9M−P), suggesting restoration of a pro-senescent inflammatory niche. Recombinant S100A8 protein

wide H3K4me3 distribution in Vehicle *versus* oridonin-treated samples. (F) GO enrichment analysis of genes with increased H3K4me3 following oridonin treatment highlights overrepresentation of NAD-related metabolic processes. (G) Visualization of H3K4me3 ChIP-seq peaks at the *Sirt2* promoter region in *Tet2*$^{+/-}$ BMT mice. (H) Transcriptome-based transcription factor enrichment analysis for STAT family members. (I) Motif enrichment analysis of promoter regions with oridonin-induced H3K4me3 reveals strong enrichment for STAT5A and STAT2 binding motifs, with high promoter coverage and centrality scores. Clusters 3−7 are enriched for anti-aging and oxidative stress−related genes.

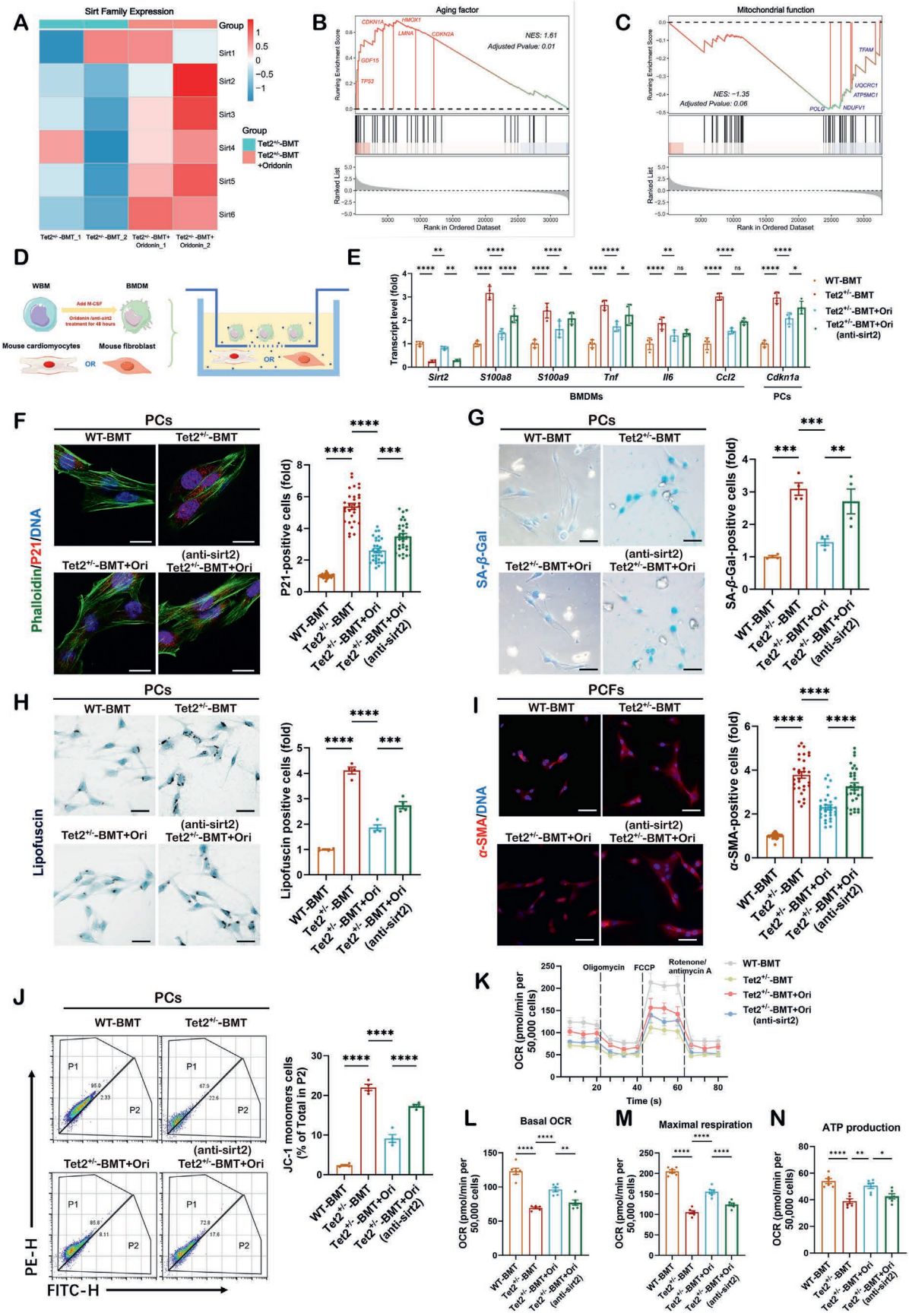
A
Sirt Family Expression
Group
Sirt1
Sirt2
Sirt3
Sirt4
Sirt5
Sirt6
Tet2+/- -BMT_1
Tet2+/- -BMT_2
Tet2+/- -BMT+ Oridonin_1
Tet2+/- -BMT+ Oridonin_2
Tet2+/-BMT
Tet2+/-BMT +Oridonin
B
Aging factor
CDKN1A
HMOX1
LMNA
CDKN2A
GDF15
TP53
NES: 1.61
Adjusted Pvalue: 0.01
Running Enrichment Score
Ranked List
Rank in Ordered Dataset
C
Mitochondrial function
TFAM
UQCRC1
ATP5MC1
NDUFV1
POLG
NES: −1.35
Adjusted Pvalue: 0.06
D
WBM
BMDM
Add M-CSF
Oridonin /anti-sirt2 treatment for 48 hours
Mouse cardiomyocytes
Mouse fibroblast
OR
E
Transcript level (fold)
WT-BMT
Tet2+/-BMT
Tet2+/-BMT+Ori
Tet2+/-BMT+Ori (anti-sirt2)
Sirt2
S100a8
S100a9
Tnf
Il6
Ccl2
Cdkn1a
BMDMs
PCs
F
PCs
WT-BMT
Tet2+/-BMT
Tet2+/-BMT+Ori
(anti-sirt2) Tet2+/-BMT+Ori
Phalloidin/P21/DNA
P21-positive cells (fold)
G
SA-β-Gal
SA-β-Gal-positive cells (fold)
H
Lipofuscin
Lipofuscin positive cells (fold)
I
PCFs
α-SMA/DNA
α-SMA-positive cells (fold)
J
P1
P2
PE-H
FITC-H
JC-1 monomers cells (% of Total in P2)
K
Oligomycin
FCCP
Rotenone/ antimycin A
OCR (pmol/min per 50,000 cells)
Time (s)
L
Basal OCR
M
Maximal respiration
N
ATP production

further aggravated mitochondrial dysfunction in cardiomyocytes, indicating amplification of SIRT2-related metabolic impairment (Supporting Information Fig. S20). Consistently, AAV9-mediated *S100A8* overexpression in *Tet2*$^{+/-}$BMT mice reproduced the pro-senescent and pro-inflammatory effects observed *in vivo*, confirming that these outcomes are intrinsic to S100A8 (Supporting Information Fig. S21).

In summary, these findings identify S100A8 as a pivotal downstream mediator of *Tet2*-CHIP-induced cardiac aging. Oridonin ameliorates aging-related cardiac remodeling and dysfunction by dampening S100A8-driven SASP.

4. Discussion

In this study, we demonstrate that TET2-driven CHIP reflects biological aging while concurrently accelerating cardiac dysfunction. Previous investigations have primarily attributed the association between CHIP, CVD and aging to immune dysregulation and systemic inflammation[8,15,38,46]. Our findings extend this framework by showing that hematopoietic *Tet2* deficiency directly promotes myocardial senescence and fibrosis, even in the absence of overt cardiovascular stress. This intrinsic ability of CHIP to drive cardiac aging phenotypes establishes a mechanistic connection between hematopoietic mutations and age-related myocardial remodeling, thereby highlighting clonal hematopoiesis as a novel target for therapeutic strategies aimed at mitigating cardiac aging and its clinical consequences.

While previous studies have primarily examined the role of clonal hematopoiesis in accelerating atherosclerosis[22,47] or worsening established cardiovascular injury[10,11,48], the contribution of CHIP to intrinsic cardiac aging phenotypes has remained largely unexplored. By demonstrating that hematopoietic *Tet2* deficiency promotes myocardial senescence and fibrosis even in the absence of overt cardiovascular stress, our study advances the understanding of CHIP beyond its role as a disease accelerator and identifies it as a potential independent driver of cardiac aging. This conceptual advance reinforces the mechanistic link between hematopoietic mutations and cardiovascular aging, thereby broadening the disciplinary framework of aging research. Furthermore, our findings that oridonin ameliorates CHIP-driven cardiac aging highlight the translational potential of this natural compound. Oridonin exerts pleiotropic anti-inflammatory, anti-fibrotic, and anti-oxidative effects, properties that may be particularly advantageous in the multifactorial context of cardiac aging. By linking hematopoietic mutations to intrinsic cardiac aging and demonstrating pharmacological rescue with oridonin, this work delineates a new mechanistic axis and highlights a promising avenue for intervention.

Modeling clonal hematopoiesis under conditions that faithfully recapitulate natural aging presents substantial technical and interpretive challenges. Clinically relevant CHIP develops slowly over many months to years[49], and reproducing this temporal dynamic in mice requires long-term follow-up after hematopoietic manipulation. In our study, we therefore monitored *Tet2*$^{+/-}$BMT mice for up to 12 months post-transplant, which allowed us to capture late-onset effects that shorter studies can miss: while prior reports observed only modest clone expansion in heterozygotes at 8 months[36], we documented a pronounced clonal expansion after 8 months that became clearly manifest by 12 months. Using heterozygous *Tet2* deficiency also has biological relevance, heterozygous mutations are common in human CHIP[19], but produces subtler and slower phenotypes that demand extended observation and larger cohorts to achieve statistical power[50]. Finally, we deliberately employed a non-myeloablative transplantation protocol to preserve the recipient's native marrow microenvironment; although this approach reduces the artificial selection pressures introduced by full myeloablation, it increases inter-animal variability and requires careful controls (*e.g.*, WT → WT-BMT) to exclude procedure-related effects. Together, these factors, long latency, modest early phenotypes in heterozygotes, late explosive clonal expansion, and the choice to retain endogenous niche signals, define key obstacles to modeling age-related clonal hematopoiesis, but they also increase the physiological fidelity of the model and strengthen the translational relevance of our findings.

Our study established a causal framework wherein *TET2*-mediated CHIP promotes cardiac aging through biased differentiation of hematopoietic stem cells into pro-inflammatory monocytes and macrophages. MR analysis supported a direct link between CHIP and age-related cardiovascular traits diseases in humans, while myocardial transcriptomes revealed selective enrichment of monocyte/macrophage signatures in CHIP carriers. These human data are functionally corroborated in our *Tet2*$^{+/}$

Figure 8 Validation of oridonin's effect in mitigating *Tet2* mutation-driven CHIP cardiac aging *via* Sirt2 activation. (A) Differential expression of *Sirt* family members in the hearts of aged mice before and after oridonin treatment. GSEA plots showing DEGs associated with aging factors (B) and mitochondrial function (C) in GSE248894 treated with Sirt2 inhibitors. (D) Schematic diagram of the co-culture system. (E) RT-qPCR analysis showing the relative expression levels of *S100a8*, *S100a9*, *Tnf*, *Il6*, and *Ccl2* in BMDMs, *Cdkn1a* in primary cardiomyocytes (PCs) following co-culture treated with oridonin or Sirt2 inhibitors. (F) Representative images (left) and quantification (right) of P21 (red) and phalloidin (green) staining in mouse PCs ($n = 30$ cells). P21 expression was quantified by mean fluorescence intensity using automated, unbiased analysis. Scale bar, 15 μm. (G) Representative images (left) and quantification (right) of SA-β-Gal staining in mouse PCs ($n = 100$ cells from four independent experiments). Scale bar, 50 μm. (H) Representative images (left) and quantification (right) of lipofuscin deposition in mouse PCs, assessed by Schmorl iron reduction ($n = 100$ cells from four independent experiments). Scale bar, 50 μm. (I) Representative images (left) and quantification (right) of α-SMA (red) expression in primary cardiac fibroblasts (PCFs; $n = 30$ cells). Scale bar, 50 μm. (J) Mitochondrial membrane potential in PCs analyzed *via* JC-1 staining and flow cytometry. Right: quantification of JC-1 monomer-positive cells ($n = 4$ independent experiments). (K) Mitochondrial respiration analysis of PCs using the Seahorse platform. (L–N) Quantification of basal oxygen consumption rate (OCR), maximal respiration, and ATP production. Data are presented as mean ± SEM. Statistical analysis by one-way ANOVA with Tukey's *post hoc* test. $^{*}P < 0.05$, $^{**}P < 0.01$, $^{***}P < 0.001$, $^{****}P < 0.0001$. Abbreviations: WBM, whole bone marrow; BMDM, bone marrow-derived macrophages; PCs, primary cardiomyocytes; PCFs, primary cardiac fibroblasts; Ori, oridonin; BMT, bone marrow transplantation; ns, not significant.

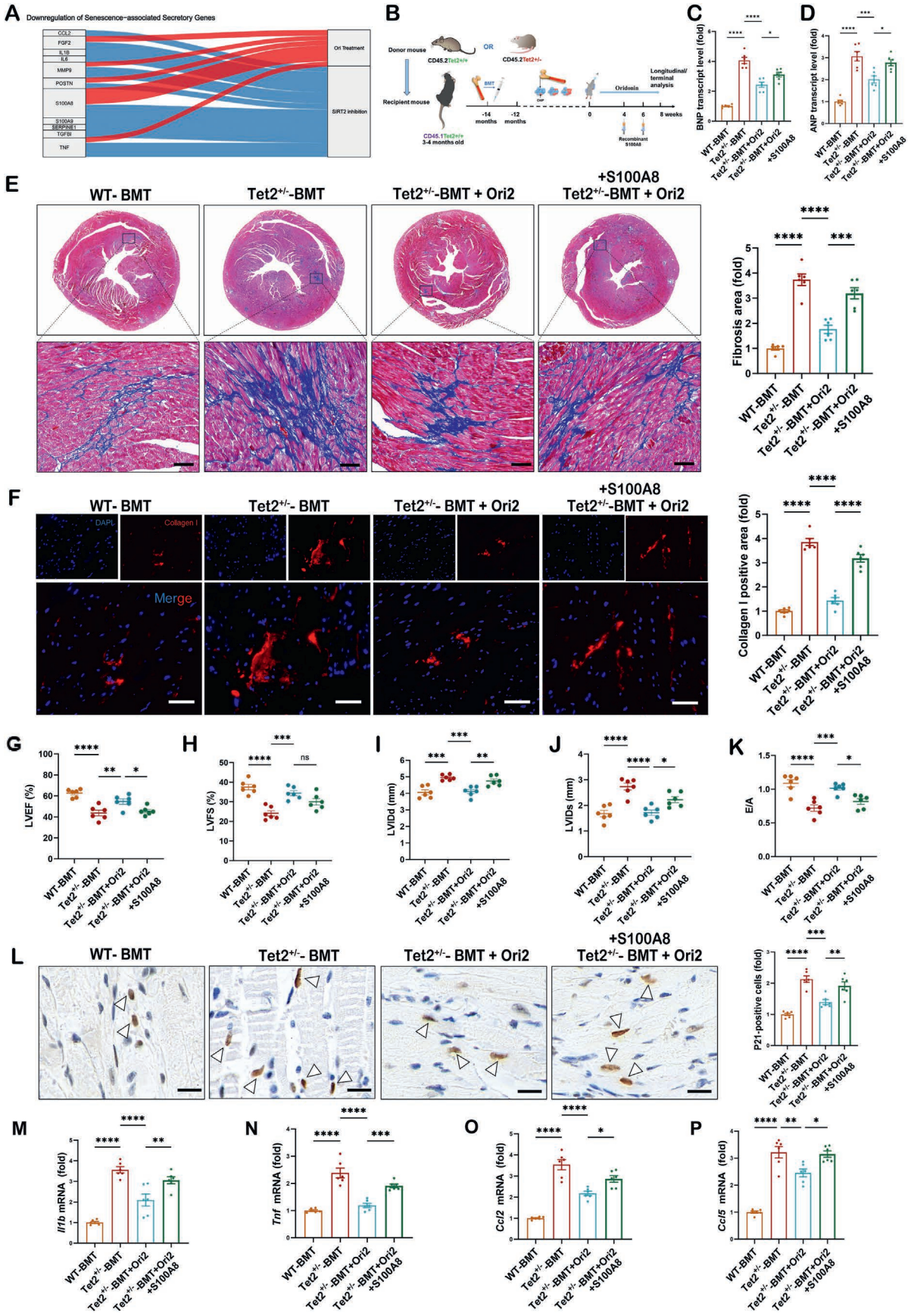
A
Downregulation of Senescence−associated Secretory Genes
CCL2
FGF2
IL1B
IL6
MMP9
POSTN
S100A8
S100A9
SERPINE1
TGFBI
TNF
Ori Treatment
SIRT2 inhibition
B
Donor mouse
CD45.2Tet2+/+
OR
CD45.2Tet2+/-
Recipient mouse
CD45.1Tet2+/+
3-4 months old
BMT
CSF
Oridonin
Recombinant S100A8
-14 months
-12 months
0
4
6
8 weeks
Longitudinal/ terminal analysis
C
BNP transcript level (fold)
D
ANP transcript level (fold)
WT-BMT
Tet2+/- -BMT
Tet2+/- -BMT+Ori2
Tet2+/- -BMT+Ori2 +S100A8
E
WT- BMT
Tet2+/-BMT
Tet2+/-BMT + Ori2
+S100A8
Tet2+/-BMT + Ori2
Fibrosis area (fold)
F
WT- BMT
Tet2+/- BMT
Tet2+/- BMT + Ori2
+S100A8
Tet2+/-BMT + Ori2
DAPI
Collagen I
Merge
Collagen I positive area (fold)
G
LVEF (%)
H
LVFS (%)
I
LVIDd (mm)
J
LVIDs (mm)
K
E/A
L
WT- BMT
Tet2+/- BMT
Tet2+/- BMT + Ori2
+S100A8
Tet2+/- BMT + Ori2
P21-positive cells (fold)
M
Il1b mRNA (fold)
N
Tnf mRNA (fold)
O
Ccl2 mRNA (fold)
P
Ccl5 mRNA (fold)

$^{-}$BMT model, in which myeloid-biased clonal expansion gives rise to macrophages exhibiting SASP activation and paracrine pro-aging effects on cardiac tissue. Together, these findings indicate that mutant hematopoiesis does not merely reflect systemic aging but actively remodels the immune landscape to accelerate cardiac dysfunction. These results were consistent with prior studies showing that *Tet2*-deficient myeloid cells exacerbate cardiac injury *via* inflammasome and IL1β signaling[11], and that age-associated clonal expansion skews myeloid fate toward inflammatory states[51] and promotes inflammatory differentiation of macrophages[22,52], suggesting that CHIP-associated macrophages appear transcriptionally distinct from those seen in physiological aging. Moreover, these observations reinforce the concept that CHIP-induced immune remodeling, particularly *via* SASP-potentiating macrophages, is a key mediator of premature cardiac aging and an actionable target for intervention.

Through a transcriptome-informed compound screen, we identified oridonin as a candidate small molecule capable of reversing *Tet2* mediated CHIP- and aging-associated transcriptomic signatures. In addition to showing comparable efficacy to dapagliflozin, oridonin may offer unique advantages as a therapeutic candidate. Oridonin is a bioactive diterpenoid isolated from *Rabdosia rubescens*, with well-documented anti-inflammatory, anti-fibrotic, and anti-proliferation in various preclinical models[25,53,54], but its potential role in mitigating cardiac aging had not been elucidated. These pleiotropic properties may be particularly relevant for age-associated cardiac remodeling, where chronic inflammation and fibrosis are key drivers of functional decline[55]. Furthermore, as a naturally derived small molecule, oridonin provides a structurally novel scaffold that differs from glucose-lowering drugs, thereby broadening the potential therapeutic landscape. Our *in vivo* safety evaluation using serum biochemical assays and histological analyses demonstrated that oridonin was well tolerated at the effective doses, further supporting its potential for translational development. We show that oridonin targets KDM5C, a JmjC domain-containing histone demethylase that removes H3K4me3, a mark associated with transcriptional activation[56]. At the same time, we do not exclude ancillary contributions from other KDM5 isoforms. Consistent with family biology, pan-KDM5 inhibition generally increases global H3K4me3, so any residual activity on other isoforms would act in the same mechanistic direction rather than against it. While the biochemical potency and genetic rescue data support KDM5C as the central mechanistic axis, cooperative but secondary contributions from other isoforms (*e.g.*, KDM5A/B/D) remain possible. In ChIP-seq and mRNA-seq, elevated *Kdm5c* expression correlated with global loss of H3K4me3 at promoters of key anti-aging genes including *Sirt2*, *Prkaa1*, and *Nfe2l2*, aligning with prior findings that age-related erosion of H3K4me3 is linked to epigenetic silencing and stress susceptibility[57,58]. Oridonin treatment or *Kdm5c* knockdown restored H3K4me3 deposition, particularly at STAT5A/STAT2-enriched loci, and activated transcriptional programs associated with stress resilience. This mechanism provides *in vivo* evidence supporting previous transcriptomic predictions of STAT-driven epigenetic control in senescence[59]. S100A8/S100A9 accumulation have previously been identified as hallmarks of aged cells and promoters of inflammatory amplification in aging tissues[60]. Among downstream targets, SIRT2 emerged as a functional effector whose activation was associated with reduced expression of S100A8. This aligns with prior work demonstrating SIRT2's role in modulating mitochondrial homeostasis and repressing SASP components[61]. Previous studies have identified SIRT2 as a nodal regulator in primate cardiac senescence and suggested its therapeutic potential in combating aging-induced cardiac hypertrophy and other age-related cardiovascular diseases[45]. Our study shows that oridonin selectively enhances SIRT2 activation through H3K4me3 enrichment, whereas other sirtuins such as *Sirt1* and *Sirt6* exhibit minimal transcriptional changes in *Tet2*$^{+/-}$BMT myeloid cells and extends this understanding by confirming that oridonin-mediated H3K4me3 enrichment activate SIRT2 to suppress S100A8, and that enforced re-expression of S100A8 attenuates the therapeutic benefits of oridonin in CHIP mice. These data define a functionally relevant KDM5C−SIRT2−S100A8 regulatory axis that connects histone methylation modification to anti-SASP outcomes.

5. Conclusions

In conclusion, this study provides mechanistic and translational insight into how *Tet2*−CHIP accelerates heart aging through a coordinated network of inflammatory, fibrosis, and epigenetic perturbations. By integrating population-scale genetics, CHIP-relevant animal models, and chromatin-level analyses, we delineate a mutation-specific aging trajectory that is distinct from physiological senescence. Importantly, we identify oridonin as a dual-action compound that targets the KDM5C−SIRT2−S100A8 axis, restoring H3K4me3 enrichment circuits while suppressing SASP amplification. These findings extend current models of heart

Figure 9 Recombinant S100A8 reverses the cardioprotective effects of oridonin in *Tet2*$^{+/-}$BMT mice. (A) Sankey diagram illustrating the relationships among cardiac aging-related factors in aged *Tet2*$^{+/-}$-BMT mice treated with oridonin. (B) Schematic of the experimental design. (C, D) RT-qPCR analysis of *Bnp* and *Anp* mRNA expression levels in BMT mouse hearts. (E) Masson's trichrome staining of heart sections from BMT mice. Left: representative images (scale bar, 50 μm). Right: quantification of fibrotic area. (F) Immunofluorescence staining for collagen 1 in BMT mouse hearts. Left: representative images (scale bar, 50 μm). Right: quantification of relative fluorescence intensity. (G−K) Representative echocardiographic quantification of cardiac function parameters, including LVEF, LVFS, LVIDd, LVIDs, and E/A ratio. (L) Immunohistochemical analysis of P21 expression in BMT mouse hearts. Left: representative images (scale bar, 20 μm). Right: quantification of P21-positive cells. (M−P) RT-qPCR analysis of *Il1b*, *Tnf*, *Ccl2*, and *Ccl5* expression in BMT mouse hearts following treatment with oridonin or S100A8 protein. Data are shown as mean ± SEM. Statistical significance determined by one-way ANOVA with Tukey's p*ost hoc* test. $^{*}P < 0.05$, $^{**}P < 0.01$, $^{***}P < 0.001$, $^{****}P < 0.0001$. Abbreviations: Ori, oridonin; BMT, bone marrow transplantation; LVEF, left ventricular ejection fraction; LVFS, left ventricular fractional shortening; E/A ratio, peak early diastolic to late atrial filling velocity; LVIDd, left ventricular internal diameter at diastole; LVIDs, left ventricular internal diameter at systole; ns, not significant.

aging and establish a conceptual foundation for mutation-informed, histone methylation modification interventions to mitigate age-related heart dysfunction in CHIP carriers.

Acknowledgments

This work was supported by a grant from the National Science Foundation of China (82374406, 82505436, and 82205236), China Postdoctoral Science Foundation (2025M783960), Guangzhou University of Chinese Medicine's Youth Elite Talents Cultivation "List Unveiling and Leadership"Team Project, The Funding Project from Guangdong Provincial Department of Education (2024KTSCX114, China), Guangzhou Science and Technology Plan Project (2025A04J5311, China), Guangdong Provincial Medical Scientific Research Foundation (B2025119, China), Young Talent Support Project of Guangzhou Association for Science and Technology (QT-2025-037, China), Guangdong Provincial Administration of Traditional Chinese Medicine (20264102), Guangzhou University of Chinese Medicine−Foundational Discipline Capacity Enhancement Initiative (Solid Foundation Project, GZY2025GB0104, China).

Author contributions

Xingling Chen and Qiangqiang Zhao: Writing − original draft, Methodology, Formal analysis, Conceptualization. Linhuang Chen and Shengrong Lin: Investigation, Data curation. Bin Mai, Xingling He, Xiaojiao Zhang and Jiahui Chen: Investigation, Data curation. Sijing Li, Ziru Li, Hua Zhang, Xiaofang Li, Yuehui Zhou and Huili Liao: Validation, Investigation. Taochun Ye, Shuning Sun, Zhongqi Yang and Shihao Ni: Supervision, Funding acquisition, Conceptualization. Lu Lu: Writing − review & editing, Supervision, Funding acquisition, Conceptualization.

Conflicts of interest

The authors declare no conflicts of interest.

Appendix A. Supporting information

Supporting information to this article can be found online at https://doi.org/10.1016/j.apsb.2026.02.006.

References

1. North BJ, Sinclair DA. The intersection between aging and cardiovascular disease. *Circ Res* 2012;**110**:1097−108.
2. Zhang Y, Ding Y, Li M, Yuan J, Yu Y, Bi X, et al. MicroRNA-34c-5p provokes isoprenaline-induced cardiac hypertrophy by modulating autophagy *via* targeting ATG4B. *Acta Pharm Sin B* 2022;**12**:2374−90.
3. Lakatta EG, Levy D. Arterial and cardiac aging: major shareholders in cardiovascular disease enterprises: part II: the aging heart in health: links to heart disease. *Circulation* 2003;**107**:346−54.
4. Stern S, Behar S, Gottlieb S. Cardiology patient pages. Aging and diseases of the heart. *Circulation* 2003;**108**:e99−101.
5. Dai DF, Chen T, Johnson SC, Szeto H, Rabinovitch PS. Cardiac aging: from molecular mechanisms to significance in human health and disease. *Antioxidants Redox Signal* 2012;**16**:1492−526.
6. Mahmoudi S, Xu L, Brunet A. Turning back time with emerging rejuvenation strategies. *Nat Cell Biol* 2019;**21**:32−43.
7. Jaiswal S, Natarajan P, Silver AJ, Gibson CJ, Bick AG, Shvartz E, et al. Clonal hematopoiesis and risk of atherosclerotic cardiovascular disease. *N Engl J Med* 2017;**377**:111−21.
8. Evans MA, Walsh K. Clonal hematopoiesis, somatic mosaicism, and age-associated disease. *Physiol Rev* 2023;**103**:649−716.
9. Fuster JJ, Walsh K. Somatic mutations and clonal hematopoiesis: unexpected potential new drivers of age-related cardiovascular disease. *Circ Res* 2018;**122**:523−32.
10. Sano S, Oshima K, Wang Y, Katanasaka Y, Sano M, Walsh K. CRISPR-Mediated gene editing to assess the roles of Tet 2 and Dnmt3a in clonal hematopoiesis and cardiovascular disease. *Circ Res* 2018;**123**:335−41.
11. Sano S, Oshima K, Wang Y, MacLauchlan S, Katanasaka Y, Sano M, et al. Tet2-mediated clonal hematopoiesis accelerates heart failure through a mechanism involving the IL-1β/NLRP3 inflammasome. *J Am Coll Cardiol* 2018;**71**:875−86.
12. Min KD, Polizio AH, Kour A, Thel MC, Walsh K. Experimental ASXL1-mediated clonal hematopoiesis promotes inflammation and accelerates heart failure. *J Am Heart Assoc* 2022;**11**:e026154.
13. Sano S, Wang Y, Ogawa H, Horitani K, Sano M, Polizio AH, et al. TP53-mediated therapy-related clonal hematopoiesis contributes to doxorubicin-induced cardiomyopathy by augmenting a neutrophil-mediated cytotoxic response. *JCI Insight* 2021;**6**:e146076.
14. Sano S, Wang Y, Yura Y, Sano M, Oshima K, Yang Y, et al. JAK2 (V617F)-mediated clonal hematopoiesis accelerates pathological remodeling in murine heart failure. *JACC Basic Transl Sci* 2019;**4**: 684−97.
15. Jaiswal S, Fontanillas P, Flannick J, Manning A, Grauman PV, Mar BG, et al. Age-related clonal hematopoiesis associated with adverse outcomes. *N Engl J Med* 2014;**371**:2488−98.
16. Jaiswal S, Libby P. Clonal haematopoiesis: connecting ageing and inflammation in cardiovascular disease. *Nat Rev Cardiol* 2020;**17**: 137−44.
17. Oren O, Small AM, Libby P. Clonal hematopoiesis and atherosclerosis. *J Clin Investig* 2024;**134**:e180066.
18. Zuriaga MA, Yu Z, Matesanz N, Truong B, Ramos-Neble BL, Asensio-Lopez MC, et al. Colchicine prevents accelerated atherosclerosis in TET2-mutant clonal haematopoiesis. *Eur Heart J* 2024;**45**: 4601−15.
19. Cochran JD, Yura Y, Thel MC, Doviak H, Polizio AH, Arai Y, et al. Clonal hematopoiesis in clinical and experimental heart failure with preserved ejection fraction. *Circulation* 2023;**148**:1165−78.
20. Abplanalp WT, Cremer S, John D, Hoffmann J, Schuhmacher B, Merten M, et al. Clonal hematopoiesis-driver DNMT3A mutations alter immune cells in heart failure. *Circ Res* 2021;**128**:216−28.
21. Assmus B, Cremer S, Kirschbaum K, Culmann D, Kiefer K, Dorsheimer L, et al. Clonal haematopoiesis in chronic ischaemic heart failure: prognostic role of clone size for DNMT3A- and TET2-driver gene mutations. *Eur Heart J* 2021;**42**:257−65.
22. Fuster JJ, MacLauchlan S, Zuriaga MA, Polackal MN, Ostriker AC, Chakraborty R, et al. Clonal hematopoiesis associated with TET2 deficiency accelerates atherosclerosis development in mice. *Science* 2017;**355**:842−7.
23. Li Y, Xie J, Du X, Chen Y, Wang C, Liu T, et al. Oridonin, a small molecule inhibitor of cancer stem cell with potent cytotoxicity and differentiation potential. *Eur J Pharmacol* 2024;**975**. 176656.
24. Zhang M, Hou L, Tang W, Lei W, Lin H, Wang Y, et al. Oridonin attenuates atherosclerosis by inhibiting foam macrophage formation and inflammation through FABP4/PPARγ signalling. *J Cell Mol Med* 2023;**27**:4155−70.
25. Wang L, Zhao X, Ding J, Liu Y, Liu H, Zheng L, et al. Oridonin attenuates the progression of atherosclerosis by inhibiting NLRP3 and activating Nrf2 in apolipoprotein E-deficient mice. *Inflammopharmacology* 2023;**31**:1993−2005.
26. Lin J, Lai X, Fan X, Ye B, Zhong L, Zhang Y, et al. Oridonin protects against myocardial ischemia−reperfusion injury by inhibiting GSDMD-mediated pyroptosis. *Genes* 2022;**13**:2133.

27. Xu M, Wan CX, Huang SH, Wang HB, Fan D, Wu HM, et al. Oridonin protects against cardiac hypertrophy by promoting P21-related autophagy. *Cell Death Dis* 2019;**10**:403.
28. Kessler MD, Damask A, O'Keeffe S, Banerjee N, Li D, Watanabe K, et al. Common and rare variant associations with clonal haematopoiesis phenotypes. *Nature* 2022;**612**:301−9.
29. McCartney DLMin JLRichmond RCLu ATSobczyk MKDavies G. Genome-wide association studies identify 137 genetic loci for DNA methylation biomarkers of aging. et al. *Genome Biol* 2021;**22**:194.
30. Backman JD, Li AH, Marcketta A, Sun D, Mbatchou J, Kessler MD, et al. Exome sequencing and analysis of 454,787 UK Biobank participants. *Nature* 2021;**599**:628−34.
31. He X, Li Z, Li S, Zhang X, Liu D, Han X, et al. Huoxue Tongluo tablet enhances atherosclerosis efferocytosis by promoting the differentiation of *Trem2*$^{+}$ macrophages *via* PPARγ signaling pathway. *Phytomedicine* 2025;**140**:156579.
32. Ni SH, Zhang XJ, OuYang XL, Ye TC, Li J, Li Y, et al. Lobetyolin alleviates ferroptosis of skeletal muscle in 5/6 nephrectomized mice *via* activation of Hedgehog−GLI1 signaling. *Phytomedicine* 2023; **115**:154807.
33. Deng JP, Liu X, Li Y, Ni SH, Sun SN, Ou-Yang XL, et al. Drug vector representation and potential efficacy prediction based on graph representation learning and transcriptome data: acacetin from traditional Chinese Medicine model. *J Ethnopharmacol* 2023;**305**:115966.
34. Ni SH, Xu JD, Sun SN, Li Y, Zhou Z, Li H, et al. Single-cell transcriptomic analyses of cardiac immune cells reveal that Rel-driven CD72-positive macrophages induce cardiomyocyte injury. *Cardiovasc Res* 2022;**118**:1303−20.
35. Ni SH, OuYang XL, Liu X, Lin JH, Li Y, Sun SN, et al. A molecular phenotypic screen reveals that lobetyolin alleviates cardiac dysfunction in 5/6 nephrectomized mice by inhibiting osteopontin. *Phytomedicine* 2022;**107**:154412.
36. Wang Y, Sano S, Yura Y, Ke Z, Sano M, Oshima K, et al. Tet2-mediated clonal hematopoiesis in nonconditioned mice accelerates age-associated cardiac dysfunction. *JCI Insight* 2020;**5**:e135204.
37. Sun SN, Ni SH, Li Y, Liu X, Deng JP, Chen ZX, et al. G-MDSCs promote aging-related cardiac fibrosis by activating myofibroblasts and preventing senescence. *Cell Death Dis* 2021;**12**:594.
38. Min KD, Kour A, Sano S, Walsh K. The role of clonal haematopoiesis in cardiovascular diseases: epidemiology and experimental studies. *J Intern Med* 2020;**288**:507−17.
39. Ma S, Sun S, Geng L, Song M, Wang W, Ye Y, et al. Caloric restriction reprograms the single-cell transcriptional landscape of rattus norvegicus aging. *Cell* 2020;**180**:984−1001.e22.
40. Gallo K, Goede A, Preissner R, Gohlke BO. SuperPred 3.0: drug classification and target prediction—a machine learning approach. *Nucleic Acids Res* 2022;**50**:W726−31.
41. Hulsmans M, Sager HB, Roh JD, Valero-Munoz M, Houstis NE, Iwamoto Y, et al. Cardiac macrophages promote diastolic dysfunction. *J Exp Med* 2018;**215**:423−40.
42. Li J, Xin Y, Wang Z, Li J, Li W, Li H. The role of cardiac resident macrophage in cardiac aging. *Aging Cell* 2023;**22**:e14008.
43. Sun SN, Ni SH, Li Y, Liu X, Deng JP, Chen ZX, et al. G-MDSCs promote aging-related cardiac fibrosis by activating myofibroblasts and preventing senescence. *Cell Death Dis* 2021;**12**:594.
44. Huang Y, He W, Zhang Y, Zou Z, Han L, Luo J, et al. Targeting SIRT2 in aging-associated fibrosis pathophysiology. *Aging Dis* 2024;**16**: 2036−53.
45. Ye Y, Yang K, Liu H, Yu Y, Song M, Huang D, et al. SIRT2 counteracts primate cardiac aging *via* deacetylation of STAT3 that silences CDKN2B. *Nat Aging* 2023;**3**:1269−87.
46. Belizaire R, Wong WJ, Robinette ML, Ebert BL. Clonal haematopoiesis and dysregulation of the immune system. *Nat Rev Immunol* 2023;**23**:595−610.
47. Gumuser ED, Schuermans A, Cho SMJ, Sporn ZA, Uddin MM, Paruchuri K, et al. Clonal hematopoiesis of indeterminate potential predicts adverse outcomes in patients with atherosclerotic cardiovascular disease. *J Am Coll Cardiol* 2023;**81**:1996−2009.
48. Rauch PJ, Gopakumar J, Silver AJ, Nachun D, Ahmad H, McConkey M, et al. Loss-of-function mutations in Dnmt3a and Tet2 lead to accelerated atherosclerosis and concordant macrophage phenotypes. *Nat Cardiovasc Res* 2023;**2**:805−18.
49. Nachun D, Lu AT, Bick AG, Natarajan P, Weinstock J, Szeto MD, et al. Clonal hematopoiesis associated with epigenetic aging and clinical outcomes. *Aging Cell* 2021;**20**:e13366.
50. Uddin MDM, Nguyen NQH, Yu B, Brody JA, Pampana A, Nakao T, et al. Clonal hematopoiesis of indeterminate potential, DNA methylation, and risk for coronary artery disease. *Nat Commun* 2022;**13**: 5350.
51. Caiado F, Kovtonyuk LV, Gonullu NG, Fullin J, Boettcher S, Manz MG. Aging drives *Tet2*$^{+/-}$ clonal hematopoiesis *via* IL-1 signaling. *Blood* 2023;**141**:886−903.
52. Yao H, He Q, Wei S, Xiang L, Luo Y, Huang C, et al. Targeted inhibition of macrophage STING signaling alleviates inflammatory injury and ventricular remodeling in acute myocardial infarction. *Acta Pharm Sin B* 2025;**15**:4030−46.
53. Gao J, Li C, Wang X, Sun X, Zhang R, Chen C, et al. Oridonin attenuates lung inflammation and fibrosis in silicosis *via* covalent targeting iNOS. *Biomed Pharmacother* 2022;**153**:113532.
54. Zhou F, Gao H, Shang L, Li J, Zhang M, Wang S, et al. Oridonin promotes endoplasmic reticulum stress *via* TP53-repressed TCF4 transactivation in colorectal cancer. *J Exp Clin Cancer Res* 2023;**42**: 150.
55. Chen J, Wei X, Zhang Q, Wu Y, Xia G, Xia H, et al. The traditional Chinese medicines treat chronic heart failure and their main bioactive constituents and mechanisms. *Acta Pharm Sin B* 2023;**13**: 1919−55.
56. Greer EL, Shi Y. Histone methylation: a dynamic mark in health, disease and inheritance. *Nat Rev Genet* 2012;**13**:343−57.
57. Sen P, Shah PP, Nativio R, Berger SL. Epigenetic mechanisms of longevity and aging. *Cell* 2016;**166**:822−39.
58. Mavromatis LA, Rosoff DB, Bell AS, Jung J, Wagner J, Lohoff FW. Multi-omic underpinnings of epigenetic aging and human longevity. *Nat Commun* 2023;**14**:2236.
59. Mallette FA, Gaumont-Leclerc MF, Ferbeyre G. The DNA damage signaling pathway is a critical mediator of oncogene-induced senescence. *Genes Dev* 2007;**21**:43−8.
60. Zhu H, Chen J, Liu K, Gao L, Wu H, Ma L, et al. Human PBMC scRNA-seq-based aging clocks reveal ribosome to inflammation balance as a single-cell aging hallmark and super longevity. *Sci Adv* 2023; **9**:eabq7599.
61. Chen JL, Feng ZL, Zhou F, Lou RH, Peng C, Ye Y, et al. 14-Deoxygarcinol improves insulin sensitivity in high-fat diet-induced obese mice *via* mitigating NF-κB/Sirtuin 2-NLRP3-mediated adipose tissue remodeling. *Acta Pharmacol Sin* 2023;**44**: 434−45.